A Loewner-Based System Identification and Structural Health Monitoring Approach for Mechanical Systems

Hindawi
Structural Control and Health Monitoring
Volume 2023, Article ID 1891062, 22 pages
https://doi.org/10.1155/2023/1891062

WILEY | Hindawi

Research Article

A Loewner-Based System Identification and Structural Health Monitoring Approach for Mechanical Systems

Gabriele Dessena,[1] **Marco Civera**,[2] **Luca Zanotti Fragonara**,[1] **Dmitry I. Ignatyev**,[1] **and James F. Whidborne**[1]

[1]*School of Aerospace, Transport and Manufacturing, Cranfield University, Cranfield, Bedfordshire MK43 0AL, UK*
[2]*Department of Structural, Geotechnical and Building Engineering, Politecnico di Torino, Turin, Piedmont 10129, Italy*

Correspondence should be addressed to Marco Civera; marco.civera@polito.it

Received 8 September 2022; Revised 11 January 2023; Accepted 27 February 2023; Published 18 April 2023

Academic Editor: Lin Chen

Data-driven structural health monitoring (SHM) requires precise estimates of the target system behaviour. In this sense, SHM by means of modal parameters is strictly linked to system identification (SI). However, existing frequency-domain SI techniques have several theoretical and practical drawbacks. This paper proposes using an input-output system identification technique based on rational interpolation, known as the Loewner framework (LF), to estimate the modal properties of mechanical systems. Pioneeringly, the Loewner framework mode shapes and natural frequencies estimated by LF are then applied as damage-sensitive features for damage detection. To assess its capability, the Loewner framework is validated on both numerical and experimental datasets and compared to established system identification techniques. Promising results are achieved in terms of accuracy and reliability.

1. Introduction

The use of vibration-based data in structural health monitoring (SHM) is an important topic, traditionally based on the identification of modal parameters [1, 2] obtained through system identification (SI). Thus, effective and precise SI is of paramount importance for damage detection, yet several alternative strategies exist for SI.

These SI methods can be divided into many categories, depending on the data domain (time or frequency) and the identification procedure (input-output or output-only). Input-output data are usually obtained by experimental modal analysis (EMA) [3], while output-only techniques are collected with operational modal analysis (OMA) techniques [4]. Recent advances have focused on frequency-domain techniques and EMA for the SHM of engineering systems [5–7]. Output-only SI was applied for monitoring multi-span bridges by Chaudhary and Fujino [8] and for arch dams by Zhi-Qian et al. [9].

In this context, the input-output SI method applied in this work is the Loewner framework (LF): an interpolation-based SI method for the model order reduction (MOR) of large-scale dynamical systems first introduced by Antoulas and co-authors in electrical engineering [10, 11].

This work aims to demonstrate the suitability of the LF [10, 11] as an efficient means for the extraction of modal parameters, by comparing it to other state-of-the-art techniques for SHM purpose and modal parameter-based damage detection, as it will be shown in the later sections of this paper. Sensitivity, accuracy, and precision of the identified modal parameters are fundamental for their use in damage detection. Therefore, the SHM problem is the perfect platform for the validation of the LF against existing and well-known SI techniques.

The main contributions of this work are as follows:

(i) The use of the LF to extract the modal parameters of mechanical systems

(ii) The application of the LF for SHM

To the best of the authors' knowledge, this is the first time these two tasks have been attempted. To this aim, the LF implementation proposed in [10–12] is modified to accommodate for the extraction of modal parameters, such as natural frequencies (ω_n), damping ratios (ζ_n), and mode shapes (ϕ_n). The goodness of the proposed method is evaluated on a numerical system, where the robustness to noise is also tested, and on a well-known experimental benchmark.

In the rest of this section, a brief recall of the two concepts of SI and SHM is given. For comparability, two well-known alternatives, numerical algorithms for subspace state-space system identification (N4SID) in the time domain and a frequency-domain version of least-squares complex exponential (LSCE) [13], are here recalled as well, before moving to the discussion of LF in the next section.

1.1. System Identification. This section focuses on *linear* SI from input-output data in the time and frequency domain. Readers interested in a more comprehensive review are directed to [14].

Subspace state-space system identification (SSI) methods, particularly N4SID, are, predominantly, time-domain methods for SI and are regarded as the state-of-the-art methods for *linear* experimental and operational modal analysis (EMA and OMA) in all fields of industrial and civil engineering. For this work, N4SID will be considered, since input-output data were used. *Linear* SSI methods, like N4SID, aim to characterise systems in the state-space form of a linear time-invariant (LTI) system under known excitation [15]:

$$\begin{aligned} \mathbf{x}_{k+1} &= \mathbf{A}\mathbf{x}_k + \mathbf{B}\mathbf{u}_k + \mathbf{w}_k \\ \mathbf{y}_k &= \mathbf{C}\mathbf{x}_k + \mathbf{D}\mathbf{u}_k + \mathbf{v}_k \\ \widehat{\mathbf{E}}\left[\begin{pmatrix}\mathbf{w}_p\\ \mathbf{v}_p\end{pmatrix}^T \begin{pmatrix}\mathbf{w}_q^T & \mathbf{v}_q^T\end{pmatrix}\right] &= \begin{pmatrix}\mathbf{Q} & \mathbf{S}\\ \mathbf{S}^{\mathbf{T}} & \mathbf{R}\end{pmatrix}\delta_{pq} \geq 0. \end{aligned} \tag{1}$$

$\mathbf{A} \in \mathbb{R}^{n\times n}$ is the system matrix, $\mathbf{B} \in \mathbb{R}^{n\times m}$ is the input matrix, $\mathbf{C} \in \mathbb{R}^{l\times n}$ is the output matrix, and $\mathbf{D} \in \mathbb{R}^{l\times m}$ is the direct feed-through matrix. m is the number of inputs, while l is the number of outputs and n is the order of the unknown system. The vectors $\mathbf{u}_k \in \mathbb{R}^{m\times 1}$ and $\mathbf{y}_k \in \mathbb{R}^{l\times 1}$ are the measurements at time instant k of, respectively, the inputs and outputs of the process. The vector $\mathbf{x}_k$ is the state vector of the process at discrete time instant k, $\mathbf{v}_k \in \mathbb{R}^{l\times 1}$ is the measurement noise, and $\mathbf{w}_k \in \mathbb{R}^{n\times 1}$ is the process noise. $\mathbf{v}_k$ and $\mathbf{w}_k$ are assumed to be zero mean, stationary white noise vector sequences and uncorrelated with the inputs $\mathbf{u}_k$. The matrices $\mathbf{Q} \in \mathbb{R}^{n\times n}$, $\mathbf{S} \in \mathbb{R}^{n\times l}$, and $\mathbf{R} \in \mathbb{R}^{l\times l}$ are the covariance matrices of $\mathbf{v}_k$ and $\mathbf{w}_k$, while $\widehat{\mathbf{E}}$ is the expected value operator and Δ_{pq} is the Kronecker delta.

In brief, the identification procedure of N4SID can be seen as a two-step process: in the first instance, the input-output data are used to develop, via projection and SVDs, the extended observability matrix and an estimate of the state sequence matrix. This, with a given set of weights specific to N4SID, is used to solve a simple set of over-determined equations, in the least-squares sense, to obtain the state-space matrices and noise model.

The interested reader is referred to [15] for the comprehensive theoretical background on SSI and N4SID. No further information on the method is provided in the remainder of the article, as N4SID is only considered a benchmark method for the scope of this article.

Another industry standard method [16] chosen for this work is a frequency-domain variant of LSCE. LSCE identification is an evolution of the complex exponential (CE) [17, 18] method that overcomes the single-input single-output (SISO) limitation of the latter, acquiring single-input multi-output (SIMO) capabilities. The LSCE implementation used within this work starts by computing, via inverse Fourier transform, the impulse response functions (IRFs) from the acquired frequency response functions (FRFs) and by fitting to the response a set of complex damped sinusoids using Prony's method, hence allowing to find the poles of the systems and its mode shapes. The interested reader is referred to [13, 19] for a more mathematical-based background of the method. The algorithms used within this work to implement N4SID and LSCE are, respectively, adaptations of MATLAB's n4sid and modalfit functions.

1.2. Structural Health Monitoring. Damage is defined as a change in a system that undermines or affects its operational capability [1]. The process of implementing a damage detection strategy for aerospace [20], civil [21], and mechanical engineering infrastructure [22] is known as structural health monitoring. SHM strategies can be divided into two categories: direct and indirect methods [23]. The latter involves model-based methods [24], and the former often relies on data-driven (especially vibration-based) strategies [2].

In the latter case, modal parameters, such as ω_n, ζ_n, and $\phi_{\mathbf{n}}$, are commonly chosen as damage indicators because they are easily identifiable from vibrational data [25] and have a direct relationship with the mass and stiffness of the target structure [2]. These can serve different purposes, for instance, damage severity assessment and damage localisation. ω_n work best for identifying the severity of the damage, but less so for the localisation, as they can easily be buried by environmental and operational variations [26] since the change in frequency is usually very small. On the other hand, $\phi_{\mathbf{n}}$ are more suited for damage localisation, which is usually done by detecting a difference between the baseline and damaged $\phi_{\mathbf{n}}$. ζ_n are usually the least-used modal parameters as a standalone damage indicator, due to their nature. In fact, ζ_n has a strong dependence on nonstructural factors, so it is difficult to define the extent of the change which is due to damage and which is not [7, 27].

For the scope of this work, ω_n is used to assess the damage severity and $\phi_{\mathbf{n}}$ is used to assess damage localisation, while ζ_n is only included to evaluate the goodness of the identification in scenarios with and without damage.

Damage quantification is obtained by computing the relative change of the corresponding ω_n between the baseline and damaged cases, while localisation is achieved by comparing the baseline and damaged ϕ_n. These approaches are well documented in the literature.

The remainder of the article is organised as follows. As anticipated, the LF theory for SI is discussed in the next section, starting from the Loewner matrix. Then, the LF is used on a numerical example, a 9 DoF system, to assess both the effect of noise on the LF identification and its sensitivity to damage. The results on the noise-free cases are also compared with N4SID and LSCE. Next, the LF SI capability is experimentally compared to N4SID and LSCE on the three-storey structure from the Engineering Institute (EI) at Los Alamos National Laboratory (LANL), where the LF is able to correctly identify modal properties and damage over the 17 cases of the dataset. Finally, the article ends with the Conclusions.

2. The Loewner Framework

Only recently has the LF been applied for SI of electrical [10, 11] and aerodynamic [28] systems. Here it is proposed for mechanical systems, in particular for the detection of modal properties and, so, for SHM purposes. To the knowledge of the authors, this has not previously been proposed. In this section, the mathematical background of the Loewner framework is provided. The discussion starts by introducing the Loewner matrix ($\mathbb{L}$) and then the Loewner pencil ($\mathbb{L}$, $\mathbb{L}_s$). Finally, the realisation problem based on the Loewner pencil is discussed. The section ends by introducing the authors' contribution to this framework.

The LF actively fits a set of frequency-domain data, in the form of FRFs, via rational interpolation, which aims at representing a given function as the quotient of two polynomials. In this case, the Loewner interpolant, matrix $\mathbb{L}$, is then used to create, or realise, a state-space representation of the data for a given order k.

The final goal does not differ from more established techniques for mechanical systems, such as rational fraction polynomial (RFP) [29], or from the recently developed [6, 7] fast relaxed vector fitting (FRVF) [30], which is an evolution of the well-known vector fitting (VF) [31]. Nevertheless, the LF's main attribute is to provide a trade-off between the accuracy of fit and complexity of the model by overcoming the severe ill-conditioning of current fitting processes [10, 32]. The LF is a *linear* SI method, despite some extensions that have recently been developed for limited nonlinear problems, such as Hammerstein cascaded dynamical systems [33]. For this work, the classic *linear* LF is considered.

2.1. The Loewner Matrix. The matrix $\mathbb{L}$ is defined as follows [34].

Given a row array of pairs of complex numbers (μ_j, ν_j), $j = 1,\ldots, q$, and a column array of pairs of complex numbers (λ_i, w_j), $i = 1,\ldots, k$, with λ_i, μ_j distinct, the associated $\mathbb{L}$, or divided-differences matrix, is

$$\mathbb{L} = \begin{bmatrix} \dfrac{\nu_1 - w_1}{\mu_1 - \lambda_1} & \cdots & \dfrac{\nu_1 - w_k}{\mu_1 - \lambda_k} \\ \vdots & \ddots & \vdots \\ \dfrac{\nu_q - w_1}{\mu_q - \lambda_1} & \cdots & \dfrac{\nu_q - w_k}{\mu_q - \lambda_k} \end{bmatrix} \in C^{q\times k}. \tag{2}$$

If there is a known underlying function ϕ, then $w_i = \phi(\lambda_i)$ and $\nu_j = \phi(\mu_j)$.

Loewner established a connection between $\mathbb{L}$ and rational interpolation, also known as Cauchy interpolation. This allows the construction of interpolants in state-space form based on the determinants of submatrices of $\mathbb{L}$ [35]. In fact, rational interpolants can be derived from $\mathbb{L}$, according to [32, 36, 37], from the Loewner pencil, and this approach is considered for the remainder of this work. The Loewner pencil comprises ($\mathbb{L}$, $\mathbb{L}_s$), where $\mathbb{L}_s$ is the *shifted Loewner matrix*, which is defined later.

The concept of interpolation and rational interpolation is not discussed further, as they are out of the main scope of this work; for further reading, the interested reader is referred to [38, 39].

2.2. The Loewner Realisation. Let us consider an LTI dynamical system Σ with m inputs and p outputs and n internal variables in descriptor-form representation which is given by

$$\boldsymbol{\Sigma}\colon \mathbf{E}\frac{d}{\mathrm{d}t}\mathbf{x}(t) = \mathbf{A}\mathbf{x}(t) + \mathbf{B}\mathbf{u}(t), \mathbf{y}(t) = \mathbf{C}\mathbf{x}(t) + \mathbf{D}\mathbf{u}(t), \tag{3}$$

where $\mathbf{x}(t) \in \mathbb{R}^n$ is the internal variable, $\mathbf{u}(t) \in \mathbb{R}^m$ is the function's input, and $y(t) \in \mathbb{R}^p$ is the output. The constant matrices are

$$\mathbf{E}, \mathbf{A} \in \mathbb{R}^{n\times n}, \mathbf{B} \in \mathbb{R}^{n\times m}, \mathbf{C} \in \mathbb{R}^{p\times n}, \mathbf{D} \in \mathbb{R}^{p\times m}. \tag{4}$$

When the matrix $\mathbf{A} - \lambda\mathbf{E}$ is nonsingular for a given finite value λ, such that $\lambda \in \mathbb{C}$, a Laplace transfer function, $\mathbf{H}(s)$, of Σ can be defined in the form of a $p \times m$ rational matrix function:

$$\mathbf{H}(s) = \mathbf{C}(s\mathbf{E} - \mathbf{A})^{-1}\mathbf{B} + \mathbf{D}. \tag{5}$$

Let us consider the more general case of tangential interpolation, also known as rational interpolation along tangential directions [40]. The right interpolation data are

$$\left.\begin{aligned} &\boldsymbol{\Lambda} = \mathrm{diag}\left[\lambda_1, \ldots, \lambda_\rho\right] \in \mathbb{C}^{\rho\times\rho} \\ &(\lambda_i; \mathbf{r}_i, \mathbf{w}_i), i = 1, \ldots, \rho \; \mathbf{R} = \begin{bmatrix}\mathbf{r}_1 & \ldots & \mathbf{r}_\rho\end{bmatrix} \in \mathbb{C}^{m\times\rho} \\ &\mathbf{W} = \begin{bmatrix}\mathbf{w}_1 & \ldots & \mathbf{w}_\rho\end{bmatrix} \in \mathbb{C}^{p\times\rho} \end{aligned}\right\}. \tag{6}$$

Likewise, the left interpolation data are

$$\left.\begin{aligned} &\mathbf{M} = \mathrm{diag}\left[\mu_1, \ldots, \mu_q\right] \in \mathbb{C}^{q\times q} \\ &\left(\mu_j, \mathbf{l}_j, \mathbf{v}_j\right), j = 1, \ldots, q \; \mathbf{L}^T = \begin{bmatrix}\mathbf{l}_1 & \ldots \mathbf{l}_q\end{bmatrix} \in \mathbb{C}^{p\times q} \\ &\mathbf{V}^T = \begin{bmatrix}\mathbf{v}_1 & \ldots & \mathbf{v}_q\end{bmatrix} \in \mathbb{C}^{m\times q} \end{aligned}\right\}. \tag{7}$$

λ_i and μ_j are the index values s at which the dataset ($\mathbf{R}$ and $\mathbf{L}$) is sampled to produce the approximation $\mathbf{H}(s)$, and ρ and q are, respectively, the dimensions of the left and right data. The vectors $\mathbf{r}_i$ and $\mathbf{l}_j$ are, respectively, the right and left tangential general directions, which are selected randomly in practice [28]. $\mathbf{w}_i$ and $\mathbf{v}_j$ are the right and left tangential data. The rational interpolation problem is solved when the transfer function $\mathbf{H}$, associated with realisation Σ in equation (3), is linked to $\mathbf{w}_i$ and $\mathbf{v}_j$:

$$\mathbf{H}(\lambda_i)\mathbf{r}_i = \mathbf{w}_i, j = 1.\ldots,\rho \text{ and } \mathbf{l}_i\mathbf{H}\left(\mu_j\right) = \mathbf{v}_j, i = 1,\ldots,q, \tag{8}$$

such that equation (8) is satisfied via the Loewner pencil.

Now, for a set of points $\mathbf{Z} = \{z_1,\ldots,z_N\}$ within the complex plane, the corresponding values of $\mathbf{H}(s)$ can be divided into the left and right data:

$$\mathbf{Z} = \left\{\lambda_1,\ldots,\lambda_\rho\right\} \cup \left\{\mu_1,\ldots,\mu_q\right\}, \tag{9}$$

with $N = q + \rho$; hence, the matrix $\mathbb{L}$ becomes

$$\mathbb{L} = \begin{bmatrix} \dfrac{\mathbf{v}_1\mathbf{r}_1 - \mathbf{l}_1\mathbf{w}_1}{\mu_1 - \lambda_1} & \cdots & \dfrac{\mathbf{v}_1\mathbf{r}_\rho - \mathbf{l}_1\mathbf{w}_\rho}{\mu_1 - \lambda_\rho} \\ \vdots & \ddots & \vdots \\ \dfrac{\mathbf{v}_q\mathbf{r}_1 - \mathbf{l}_q\mathbf{w}_1}{\mu_q - \lambda_1} & \cdots & \dfrac{\mathbf{v}_q\mathbf{r}_\rho - \mathbf{l}_q\mathbf{w}_\rho}{\mu_q - \lambda_\rho} \end{bmatrix} \in \mathbb{C}^{q\times\rho}. \tag{10}$$

Since $v_v r_p$ and $l_v w_p$ are scalars, $\mathbb{L}$ satisfies the Sylvester equation in such a fashion:

$$\mathbb{L}\mathbf{\Lambda} - \mathbf{M}\mathbb{L} = \mathbf{LW} - \mathbf{VR}. \tag{11}$$

Now, it is possible to define the *shifted Loewner matrix*, $\mathbb{L}_s$, as $\mathbb{L}$ corresponding to $sH(s)$:

$$\mathbb{L}_s = \begin{bmatrix} \dfrac{\mu_1\mathbf{v}_1\mathbf{r}_1 - \lambda_1\mathbf{l}_1\mathbf{w}_1}{\mu_1 - \lambda_1} & \cdots & \dfrac{\mu_1\mathbf{v}_1\mathbf{r}_\rho - \lambda_\rho\mathbf{l}_1\mathbf{w}_\rho}{\mu_1 - \lambda_\rho} \\ \vdots & \ddots & \vdots \\ \dfrac{\mu_q\mathbf{v}_q\mathbf{r}_1 - \lambda_1\mathbf{l}_q\mathbf{w}_1}{\mu_q - \lambda_1} & \cdots & \dfrac{\mu_q\mathbf{v}_q\mathbf{r}_\rho - \lambda_\rho\mathbf{l}_q\mathbf{w}_\rho}{\mu_q - \lambda_\rho} \end{bmatrix} \in \mathbb{C}^{q\times\rho}. \tag{12}$$

Likewise, the Sylvester equation is satisfied as follows:

$$\mathbb{L}_s\mathbf{\Lambda} - \mathbf{M}\mathbb{L}_s = \mathbf{LW}\mathbf{\Lambda} - \mathbf{MVR}. \tag{13}$$

Let us consider equation (5) and, particularly, matrix $\mathbf{D}$. As shown in [37], the $\mathbf{D}$-term is incorporated in the other matrices as it it does not influence interpolation; hence, $\mathbf{D}$ is set to 0 per convention. So, equation (5) becomes

$$\mathbf{H}(\mathrm{s}) = \mathbf{C}(\mathrm{s}\mathbf{E} - \mathbf{A})^{-1}\mathbf{B}. \tag{14}$$

A realisation of the smallest possible dimension exists only when it is completely controllable and observable. Hence, when the data are assumed to be sampled from a system for which the transfer function can be described by equation (14), the generalised tangential observability, $\mathcal{O}_q$, and generalised tangential controllability, $\mathcal{R}_\rho$, matrices can be defined from equations (13) and (14) as follows [11]:

$$\mathcal{O}_q = \begin{bmatrix} \mathbf{l}_1\mathbf{C}\left(\mu_1\mathbf{E} - \mathbf{A}\right)^{-1} \\ \vdots \\ \mathbf{l}_v\mathbf{C}\left(\mu_q\mathbf{E} - \mathbf{A}\right)^{-1} \end{bmatrix} \in \mathbb{R}^{q\times n}, \tag{15}$$

$$\mathcal{R}_\rho = \left[\left(\lambda_1\mathbf{E} - \mathbf{A}\right)^{-1}\mathbf{B}\mathbf{r}_1 \cdots \left(\lambda_\rho\mathbf{E} - \mathbf{A}\right)^{-1}\mathbf{B}\mathbf{r}_\rho\right] \in \mathbb{R}^{n\times\rho}. \tag{16}$$

Now, let us incorporate equations (15) and (16) into, respectively, equations (10) and (12):

$$\mathbb{L}_{j,i} = \frac{\mathbf{v}_j\mathbf{r}_i - \mathbf{l}_j\mathbf{w}_i}{\mu_j - \lambda_i} = \frac{\mathbf{l}_j\mathbf{H}(\mu_i)\mathbf{r}_i - \mathbf{l}_j\mathbf{H}(\lambda_i)\mathbf{r}_i}{\mu_j - \lambda_i} = -l_j\mathbf{C}\left(\mu_j\mathbf{E} - \mathbf{A}\right)^{-1}\mathbf{E}\left(\lambda_i\mathbf{E} - \mathbf{A}\right)^{-1}\mathbf{B}\mathbf{r}_i, \tag{17}$$

$$\left(\mathbb{L}_s\right)_{j,i} = \frac{\mu_j\mathbf{v}_i\mathbf{r}_i - \lambda_i\mathbf{l}_j\mathbf{w}_i}{\mu_j - \lambda_i} = \frac{\mu_j\mathbf{l}_j\mathbf{H}(\mu_i)\mathbf{r}_i - \lambda_i\mathbf{l}_j\mathbf{H}(\lambda_i)\mathbf{r}_i}{\mu_j - \lambda_i} = -\mathbf{l}_j\mathbf{C}\left(\mu_j\mathbf{E} - \mathbf{A}\right)^{-1}\mathbf{A}\left(\lambda_i\mathbf{E} - \mathbf{A}\right)^{-1}\mathbf{B}\mathbf{r}_i. \tag{18}$$

First, let us first consider the case of minimal amount of data, where it is assumed $p = v$. The assumption is based on the fact that no duplicated data are allowed in $\mathbf{R}$ and $\mathbf{L}$. Thus, rearrange equations (15) and (16) into equations (17) and (18):

$$\begin{aligned}\mathbb{L} &= -\mathcal{O}_v \mathbf{E} \mathcal{R}_\rho,\\ \mathbb{L}_s &= -\mathcal{O}_v \mathbf{A} \mathcal{R}_\rho.\end{aligned} \tag{19}$$

Then, let the Loewner pencil be a regular pencil, in the sense of $\text{eig}((\mathbb{L}, \mathbb{L}_s)) \neq (\mu_i, \lambda_i)$:

$$\begin{aligned}\mathbf{E} &= -\mathbb{L},\\ \mathbf{A} &= -\mathbb{L}_s,\\ \mathbf{B} &= \mathbf{V},\\ \mathbf{C} &= \mathbf{W}.\end{aligned} \tag{20}$$

Accordingly, the interpolating rational function is described as

$$\mathbf{H}(s) = \mathbf{W}\left(\mathbb{L}_s - s\mathbb{L}\right)^{-1}\mathbf{V}. \tag{21}$$

The aforementioned derivation refers to the minimal amount of data instance, which is rarely the case when dealing with real data. Nevertheless, the LF is extendable to redundant data. First, let us assume

$$\begin{aligned}\text{rank}\left[\boldsymbol{\zeta}\mathbb{L} - \mathbb{L}_s\right] &= \text{rank}\left[\mathbb{L}\ \mathbb{L}_s\right] == \text{rank}\begin{bmatrix}\mathbb{L}\\ \mathbb{L}_s\end{bmatrix}\\ &= k; \forall \boldsymbol{\zeta} \in \left\{\lambda_j\right\} \cup \left\{\mu_i\right\}.\end{aligned} \tag{22}$$

Secondly, the short singular value decomposition (SVD) of $\zeta\mathbb{L} - \mathbb{L}_s$ is computed:

$$\text{svd}\left(\boldsymbol{\zeta}\mathbb{L} - \mathbb{L}_s\right) = \mathbf{Y}\boldsymbol{\Sigma}_\mathbf{l}\mathbf{X}, \tag{23}$$

where $\text{rank}(\zeta\mathbb{L} - \mathbb{L}_s) = \text{ran}\quad \text{k}(\Sigma_l) = \text{size}(\Sigma_l) = k, \mathbf{Y} \in \mathbb{C}^{q\times k}$ and $\mathbf{X} \in \mathbb{C}^{k\times\rho}$, where k is the order of the approximation. Thirdly, note that

$$\begin{aligned}-\mathbf{A}\mathbf{X} + \mathbf{E}\mathbf{X}\boldsymbol{\Sigma}_\text{l} &= \mathbf{Y}^*\mathbb{L}_\text{s}\mathbf{X}^*\mathbf{X} - \mathbf{Y}^*\mathbb{L}\mathbf{X}^*\mathbf{X}\boldsymbol{\Sigma}_\text{l}\\ &= \mathbf{Y}^*\left(\mathbb{L}_\text{s} - \mathbb{L}\boldsymbol{\Sigma}_\text{l}\right) = \mathbf{Y}^*\mathbf{V}\mathbf{R} = \mathbf{B}\mathbf{R},\end{aligned} \tag{24}$$

and likewise, $-\mathbf{Y}\mathbf{A} + \mathbf{M}\mathbf{Y}\mathbf{E} = \mathbf{L}\mathbf{C}$ such that $\mathbf{X}$ and $\mathbf{Y}$ are, respectively, the generalised controllability and observability matrices for the system Σ with $\mathbf{D} = 0$.

After checking for the right and left interpolation conditions, the Loewner realisation for redundant data is

$$\begin{aligned}\mathbf{E} &= -\mathbf{Y}^*\mathbb{L}\mathbf{X},\\ \mathbf{A} &= -\mathbf{Y}^*\mathbb{L}_\text{s}\mathbf{X},\\ \mathbf{B} &= \mathbf{Y}^*\mathbf{V},\\ \mathbf{C} &= \mathbf{W}\mathbf{X}.\end{aligned} \tag{25}$$

The formulation of equation (25)—i.e., the Loewner realisation for redundant data—is going to be considered in the remainder of this work. The interested reader is referred to [32, 37] for a more in-depth discussion of each step.

2.3. The Algorithm. Having outlined the general process to characterise a system in the form of equation (25), the general application is applied to the specific case of frequency-domain data. Of particular interest is the application in [10–12] for a MIMO system. These advances were of service to the authors to develop their application to mechanical systems. Particularly, the implementation deviates from the one proposed in [10–12] as it introduces the identification of modal parameters, thus making the LF a viable instrument for the identification of modal parameters of linear mechanical systems. The implementation is outlined in Algorithm 1, and a MATLAB implementation is available from a Cranfield Online Research Data (CORD) entry [41].

In Algorithm 1, the function Loewner creates $\mathbb{L}, \mathbb{L}_s$ and the interpolation data matrices, **V** and **W**, by following the process outlined in equations (6)–(13). The data in **H** are sampled in the right and left data vectors, respectively, in such a fashion: 1 : 2 : end and 2 : 2 : end (using MATLAB notation). Then, the generalised tangential directions vectors are generated as random vectors, using the randn MATLAB function. After having established the right and left data, it is trivial, by following the abovementioned proofs, to obtain the $\mathbb{L}$, $\mathbb{L}_s$ and the interpolation data matrices, **V** and **W**, and progress in the algorithm. The main contribution and novelty of this work for the processing of vibrational signals from mechanical systems are outlined in points 7 and 8 of Algorithm 1.

2.4. Numerical Case Study. In order to investigate the goodness of fit and the effect of noise on the results of the LF-based SI, a numerically simulated 9 DoF mass-spring-damper system, as shown in Figure 1, is developed. The system consists of nine masses, such that $m_n = 1\,\text{kg}$, adjacently linked with springs, such that $k_n = 5000\,\text{Nm}^{-1}$, and dampers, characterised by the critical damping ratio of $\zeta_n = 1\%\ \forall n$. This is based on the case illustrated in [42].

The numerical model is excited with a unit (1 N) rectangular impulse applied to the first mass as input force, and the data are recorded at a sampling frequency $f_s = 200\,\text{Hz}$, with a frequency resolution of $\Delta f = 0.05\,\text{Hz}$. According to the Nyquist criterion, only frequencies up to 100 Hz are inspected; however, this is not an issue since all nine modes fall into this frequency range. The receptance FRFs are extracted by dividing the fast Fourier transform (FFT) of the output displacement recordings by the input force FFT, at each output channel (i.e., at each mass and DoF). Note that the algorithm can be applied both in a SISO or a SIMO fashion. For brevity, only the results for a SIMO application (considering all the available output channels at once) are reported and discussed.

The response of the modelled system is considered with and without artificially added additive white Gaussian noise (AWGN), to test its robustness to measurement noise. The error is calculated with respect to the known numerical results. For the idealised noise-free scenario, the LF can correctly identify ω_{1-9}, with a maximum discrepancy of 0.025%, ζ_{1-9}, and ϕ_{1-9}, demonstrated [43] with a MAC (modal assurance criterion) of unity for all modes. The MAC is computed with the usual formulation [44]:

$$\text{MAC}(\phi_b, \phi_e) = \frac{\left(\phi_\text{b} \cdot \phi_\text{e}\right)^2}{\left(\phi_\text{b} \cdot \phi_\text{b}\right)\left(\phi_\text{e} \cdot \phi_\text{e}\right)}, \tag{26}$$

Input: The system's FRFs as $\mathbf{H}(\omega)$, the frequency vector as ω, and the LF order as k.
Output: A matrix with the modal properties (ω_n, ζ_n, and ϕ_n), the Loewner realisation, and $[\mathbf{E}, \mathbf{A}, \mathbf{B}, \mathbf{C}, \mathbf{D}]$.
(1) $[\mathbb{L}, \mathbb{L}_s, \mathbf{V}, \mathbf{W}, \mu, \lambda]$ = loewner $(j\omega, H, \omega)$[11], [14];
(2) $[\mathbf{X}, \mathbf{Y}]$ = svd $(\mathbb{L})$ and enforce order k of the LF: $\mathbf{X}_k = \mathbf{X}(:, 1{:}\,k)$ and $\mathbf{Y}_k = \mathbf{Y}(:, 1{:}\,k)$;
(3) Find $[\mathbf{E}, \mathbf{A}, \mathbf{B}, \mathbf{C}]$ as per equation (25);
(4) Ensure pole stability: if necessary, turn E into an identity matrix;
(5) Set $\mathbf{D} = 0$;
(6) Obtain $[\mathbf{E}, \mathbf{A}, \mathbf{B}, \mathbf{C}, \mathbf{D}]$ and the Loewner realisation;
(7) Convert from descriptor state-space model to continuous state-space model;
(8) Compute the system poles and obtain ω_n, ζ_n, and ϕ_n.

Algorithm 1: The LF for mechanical system algorithm.

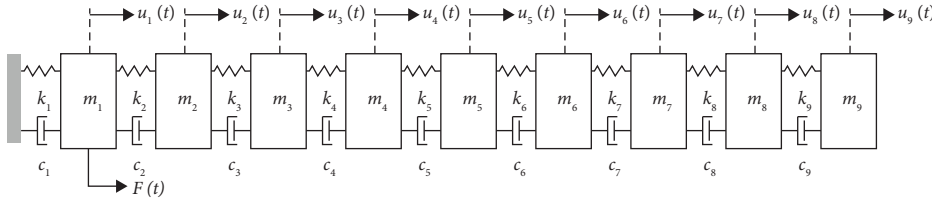

Figure 1: 9 DoF system: schematic diagram (adapted from [42]).

where b and e subscripts, respectively, represent the baseline and the mode shape to be compared.

Before introducing the investigation of noise effects in the numerical system, it is beneficial to compare the precision of LF with that of N4SID and LSCE against the known ground truth (benchmark). In Tables 1–3, ω_n, ζ_n, and ϕ_n are compared for the noiseless case.

From Tables 1–3, it is clear that the parameters identified via LF and N4SID are extremely coherent with the numerical values. In fact, N4SID is virtually identical for every parameter, while LF shows a very slight (0.025%) difference for ω_n, but perfect adherence to the numerical values for ζ_n and ϕ_n. On the other hand, LSCE performance is very poor. Errors for the ω_n identification are above 40% and 800% for ζ_n. This tendency is also confirmed for ϕ_n, for which only the first mode is acceptably coherent with the numerical results. The poor performance of LSCE could be explained by the closely spaced modes included in the dataset. Due to its computation steps, LSCE is only able to build a rank-deficient matrix and so misinterpret the closely spaced modes. As is shown later in the experimental case study, LSCE works fine for sparser modes.

It can be said that for noiseless scenarios, even for closely spaced modes, the LF can perform similarly to the most established technique, N4SID, and better than others, e.g., LSCE. This is the first step toward proving the feasibility of LF as a SI method. A test of the LF robustness to noise follows and anticipates a potential application for SHM. The same numerical system as above is used for these studies.

2.5. Investigation of Noise Effects. The effects of noise on the Loewner-based SI are numerically investigated as follows. The signal is corrupted at the input, at the output, and/or at both with a noise range between 0 and 25% with intervals of 1%, totalling 75 independent cases. The percentage of noise is defined as a fraction of the signal's standard deviation, σ. As an overall metric of fitness between the numerically derived receptance FRF and the Loewner realisation, a deviation quantity is introduced as local root mean square error (RMSE_{ij}) between the FRFs' columns at a given frequency step and is defined with the following formulation:

$$\mathrm{RMSE}_{ij} = \sqrt{\left(f_i^{fit}(j) - f_i(j)\right)\left(f_i^{fit}(j) - f_i(j)\right)^*}, \tag{27}$$

where $f_i^{\mathrm{fit}}(j)$ indicates the Loewner realisation's column at the given frequency vector index j, likewise $f_i(j)$ as the FRFs' columns at the corresponding frequency. The global root mean square error (RMSE) is then calculated with its usual formulation:

$$\mathrm{RMSE} = \sqrt{\frac{1}{I}\sum_{i=1}^{I}\frac{1}{K}\sum_{j=1}^{K}\left(f_i^{fit}(j) - f_i(j)\right)\left(f_i^{fit}(j) - f_i(j)\right)^*}, \tag{28}$$

where I is the number of FRFs' columns and the other notation is consistent with equation (27). The number of frequency points, K, is given by $f_s/2/\Delta f$, which returns 2000.

The results of the goodness of fit of the model for input-output noise equal to 0%, 1%, and 5% are presented in Figure 2. For all the aforementioned cases, as it will be discussed later in further detail, Figure 3 shows the effect of noise on the estimations of ω_n, ζ_n, and ϕ_n, while Figure 4 reports the effect of noise in terms of RMSE, per given noise level and iteration (considering five iterations).

By analysing Figure 2 in detail, the FRFs of the nine channels are superimposed for conciseness, with the numerical data represented by a blue line and the fitted model by a dashed red line. As expected, the deviation, indicated

Table 1: Natural frequencies, in Hz, identified via LF, N4SID, and LSCE and their relative difference to the numerical values.

	Natural frequency (Hz)-(relative difference-%)			
Mode	Benchmark	LF	N4SID	LSCE
#1	1.859	1.859	1.859	2.647
	—	(0.025)	(−)	(42.394)
#2	5.525	5.527	5.525	5.963
	—	(0.025)	(−)	(7.923)
#3	9.041	9.044	9.041	9.311
	—	(0.025)	(−)	(2.982)
#4	12.311	12.314	12.311	12.012
	—	(0.025)	(−)	(−2.425)
#5	15.244	15.248	15.244	15.420
	—	(0.025)	(−)	(1.150)
#6	17.762	17.766	17.762	16.144
	—	(0.025)	(−)	(−9.106)
#7	19.795	19.800	19.795	19.046
	—	(0.025)	(−)	−3.784
#8	21.288	21.294	21.288	21.705
	—	(0.025)	(−)	1.956
#9	22.201	22.206	22.201	22.694
	—	(0.025)	(−)	2.219

Table 2: Damping ratios identified via LF, N4SID, and LSCE and their relative difference to the numerical values.

	Damping ratio (−)-(relative difference-%)			
Mode	Benchmark	LF	N4SID	LSCE
#1	0.010	0.010	0.010	0.096
	—	(−)	(−)	(864.412)
#2	0.010	0.010	0.010	0.056
	—	(−)	(−)	(456.304)
#3	0.010	0.010	0.010	0.036
	—	(−)	(−)	(261.094)
#4	0.010	0.010	0.010	0.025
	—	(−)	(−)	(149.527)
#5	0.010	0.010	0.010	0.002
	—	(−)	(−)	(−81.580)
#6	0.010	0.010	0.010	0.019
—		(−)	(−)	(90.889)
#7	0.010	0.010	0.010	0.017
—		(−)	(−)	(69.254)
#8	0.010	0.010	0.010	0.013
—		(−)	(−)	(25.981)
#9	0.010	0.010	0.010	0.011
	—	(−)	(−)	(12.645)

Table 3: MAC values between the mode shapes obtained from LF, N4SID, and LSCE and the numerical value.

	MAC value (computed with respect to the benchmark) (−)			
Mode	Benchmark	LF	N4SID	LSCE
#1	1	1	1	0.979
#2	1	1	1	0.110
#3	1	1	1	0.034
#4	1	1	1	0.005
#5	1	1	1	0.110
#6	1	1	1	0.124
#7	1	1	1	0.025
#8	1	1	1	0.001
#9	1	1	1	0.018

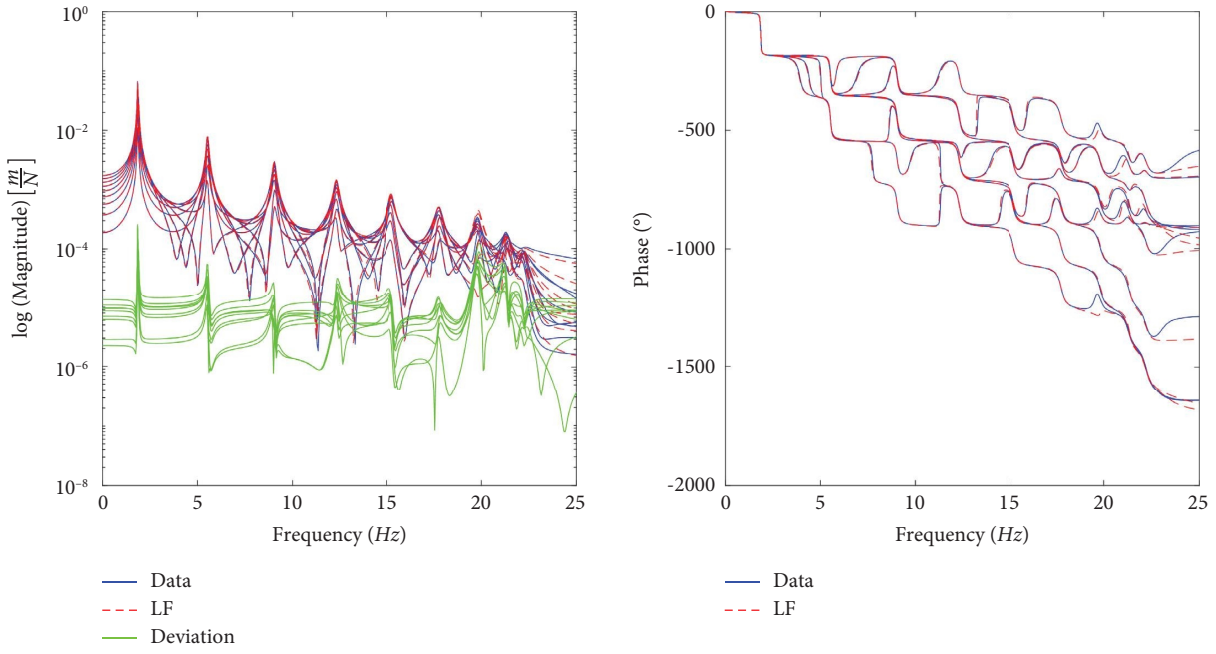

(a)

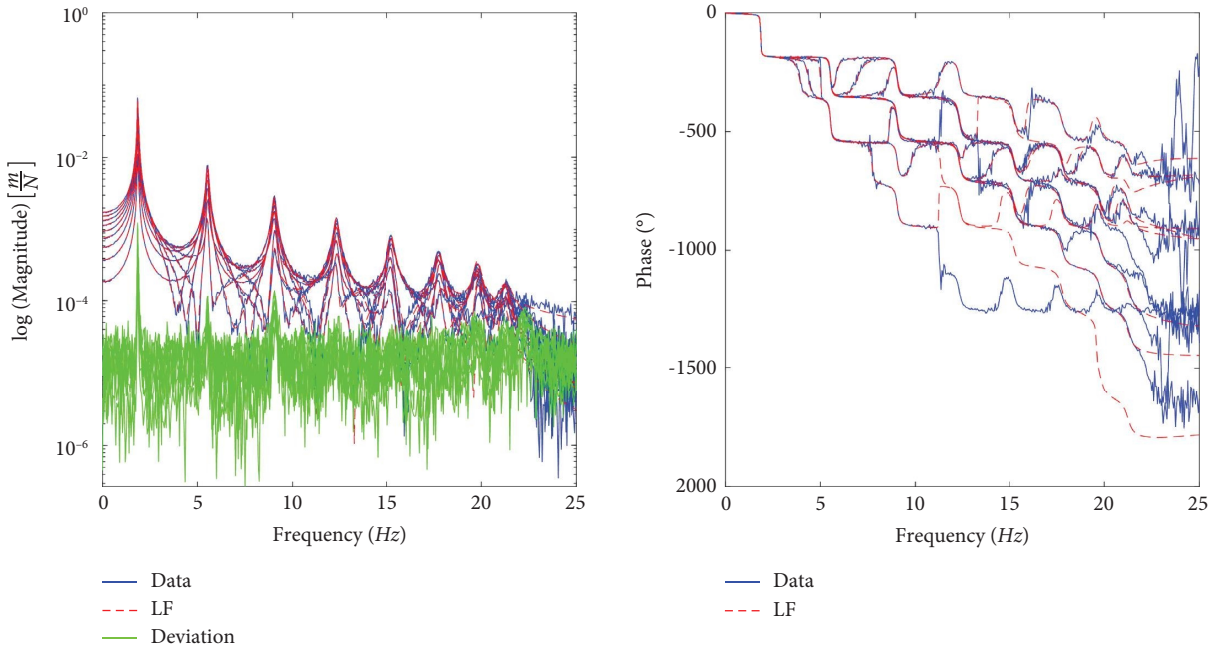

(b)

Figure 2: Continued.

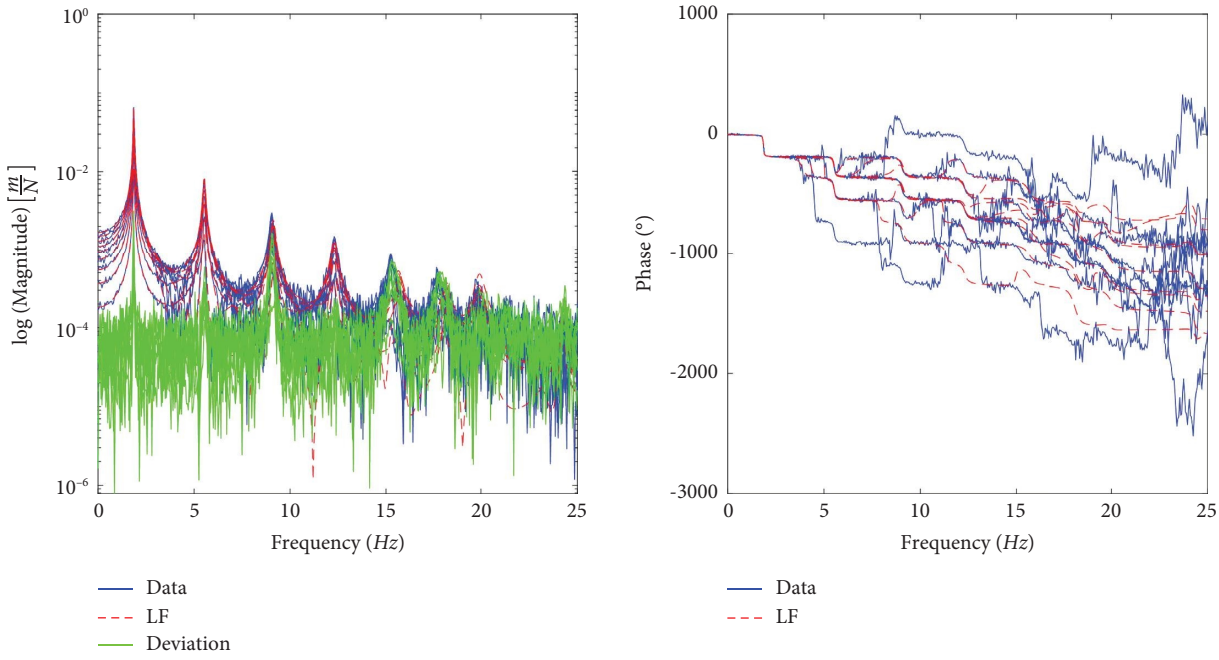

(c)

FIGURE 2: 9 DoF system: results of the numerical study on the numerical case: the 9 DoF system numerical receptance FRF is compared with LF's transfer function results for the 0% (a), 1% (b), and 5% (c) input-output noise cases. In each subfigure, from left to right, the gain's absolute value and the phase angle are presented. For conciseness, all 9 channels are superimposed.

by the green line, increases with the noise. Also, the phase accuracy decreases as the noise increases, particularly for high DoF. However, the absolute value of the deviation does not rise significantly with increasing noise, excluding the noise-free scenario. Considering these early results on a numerical model, it could be asserted that, for the LF, phase modelling is more sensitive to noise than peak amplitude. However, it should be noted, particularly with reference to Figure 2(b), that the deviation does not have a constant value. In fact, it seems linearly related to the frequency. A qualitative explanation of this phenomenon could be traced back to the nature of the LF as an interpolation matrix. The increase in deviation over frequency could be justified by the sum of multiple interpolation errors along the FRF. The minimum order case $k = 1$ (for the LF, the minimum order should be two times the number of modes to be discovered in the frequency interval) is considered in Figure 2. However, the decay in performance over noise does not constitute a problem, as shown in Figure 3, when addressing modal parameters as the order k of the Loewner realisation was raised accordingly and a stabilisation diagram was used to detect the stable poles.

Figure 3 compares the correlation between the numerical and estimated data when subjected to noise. Figures 3(a)–3(c) show the results for the case of input noise, Figures 3(d)–3(f) show the results for output noise, and Figures 3(g)–3(i) show the results for the input-output noise case. The main modal quantities, ω_n, ζ_n, and ϕ_n, were considered. ω_n and ζ_n estimation results are presented as the relative difference (Δ), in percentage, calculated by

$$\Delta = \frac{x_e - x_b}{x_b}, \tag{29}$$

where x_e and x_b represent, respectively, the estimated and baseline quantities.

As expected, the increase in noise is related to a decrease in the identification of the precision of the modal parameters by the LF. However, it should be noted that input noise has a negligible effect compared to output-only and input-output noise. As shown in Figures 3(a)–3(c), for input-only noise, the correlation between the numerical and estimated properties is almost uninfluenced by any noise level, even the most severe. Conversely, for output-only and input-output noise, ω_n are almost always correctly identified for all cases and ϕ_n always show a good correlation for the first 5 modes. ζ_n, as expected, appear to be the most problematic quantity. For any case where noise is higher than 2% and a mode higher than 3, considerable errors, exceeding 50%, are identified. Nevertheless, ζ_n are correctly identified for all modes only with 0% and 1% noise.

In Figure 4, the effect of noise on the global RMSE is investigated over five iterations, for statistical significance. It should be noted that the LF order was set to its minimum order k. As already discussed, the global RMSE of the input-only noise is considerably lower, about five times, than the output and input-output cases. In fact, while all three cases increase linearly with noise, the latter two have a very similar

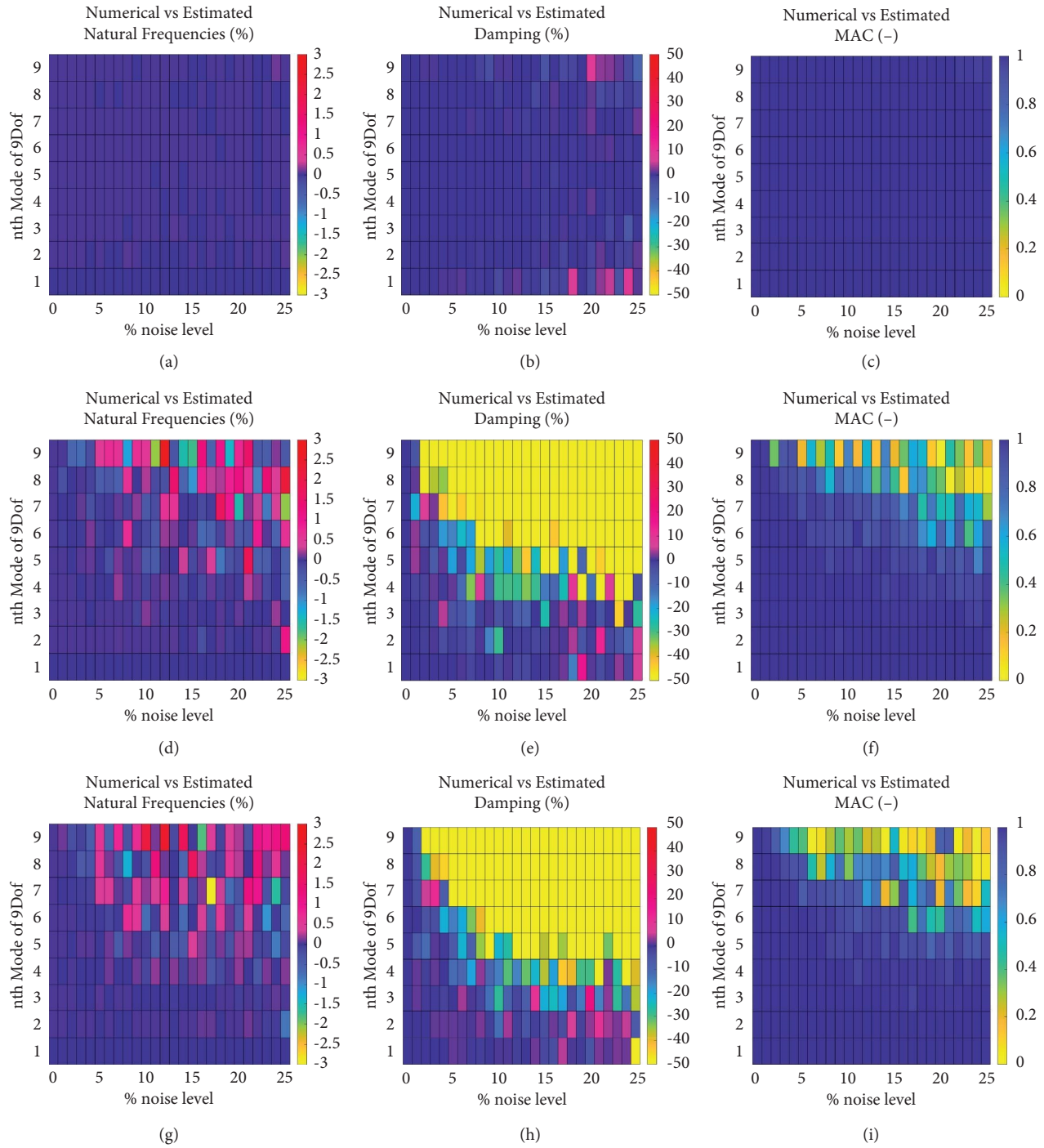

FIGURE 3: 9 DoF system: results of the numerical study. (a, b, c) Effects of input-only noise. (d, e, f) Output-only noise. (g, h, i) Input-output noise. The first column refers to the relative difference in ω_n, in %. The second column reports the same differences for ζ_n. The third column reports the MAC value as computed between the numerical and the estimated value of ϕ_n.

trend and magnitude. Hence, output noise has a greater effect on the goodness of the Loewner realisation than input noise.

Overall, the abovementioned results show that the LF is a promising method for the identification of mechanical systems. Importantly, the value of global RMSE never exceeds $5 \bullet 10^{-4}$, and Figure 3 shows that, for small enough noise values, the modal properties are correctly identified. This is also confirmed in Figure 2, where, as the level of noise increases, the fitted model deviated from the numerical data; however, this is particularly true for phase data and ζ_n, rather than amplitude, ω_n, and ϕ_n.

From these numerical results, it can be said that the LF is able to correctly identify the modal parameters of the numerical system even when it is artificially corrupted with noise. In particular, in the given study, the LF is

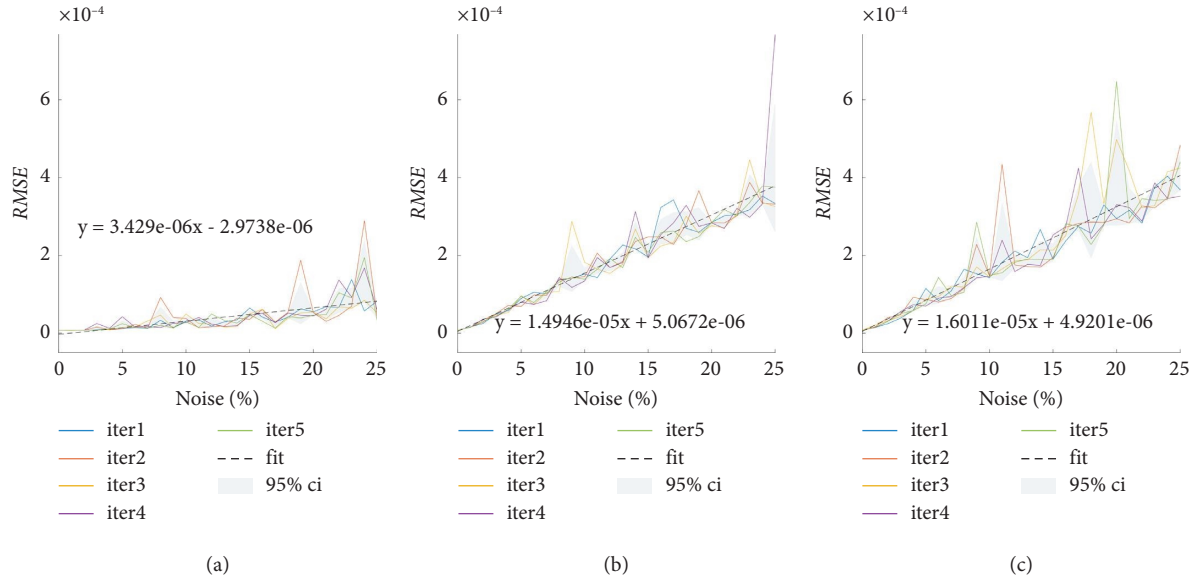

Figure 4: 9 DoF system: relationship between the noise level for input-only (a), output-only (b), and input-output (c) noise and global RMSE. 95% CI stands for 95% confidence interval.

virtually unaffected by input noise, while output-only noise and input-output noise are found to have a similar influence. Notably, the mode shapes and natural frequencies of the first three modes are always correctly identified at all noise levels. ϕ_n is the less affected parameter, followed by ω_n. ζ_n is the one relatively more affected by noise. In conclusion, LF is a suitable method, in terms of noise and precision, for the identification of the modal parameters of mechanical systems. In addition, the robustness to noise of ω_n and ϕ_n identification makes the LF sensitive enough to detect small variations under realistic conditions. This property makes it a valid candidate for the SHM of mechanical systems, as is shown in the following section.

2.6. Investigation of Damage Effects. Having assessed the capability of the LF to identify mechanical systems, this section investigates its ability to be employed as a SHM method, i.e., the capacity of the LF to detect changes in ω_n, ζ_n, and ϕ_n due to a damage condition. For this scope, the 9 DoF system shown in Figure 1 is considered. In order to simulate damage, the stiffness of the fifth element (k_6) is reduced by 5, 10, and 30%. It should be made clear that ζ_n levels, in terms of damping ratio, are not modified in the damaged system as they are heavily influenced by noise; hence, comparison on ζ_n is deferred to the experimental example in the following section. Noise is also taken into consideration; however, for SHM scope, only the input-output noise case is considered, as it is shown that input-only noise has a negligible effect and that output-only noise has a similar effect to input-output noise. The same noise intervals as in the previous section are considered, hence giving 26 cases per damage step and a total, over the three damage scenarios, of 78. The results in this section are presented by comparing the identified ω_n, in Hz, with the numerical damaged counterpart. The same is done for ζ_n.

In order to measure ϕ_n's correlation with the numerical damaged case, the MAC value between the numerical and the identified ϕ_n, computed as per equation (26), is selected as the figure of merit. Table 4 shows ω_n of the baseline and damaged numerical cases, which serves as a source of comparison with the data in Figure 5.

Figure 5 shows that the LF detects all the damaged cases correctly for all modes with noise levels less than 3%, except for ζ_n, which confirms it to be the parameter most influenced by noise. It is seen that for all noise levels and damage cases, ω_n, ζ_n, and ϕ_n show a good correlation, with the expected results, for the first four modes. In addition, ω_n and ϕ_n are well correlated for the first eight modes. A case of specific interest is the 5% stiffness reduction scenario, as it allows to demonstrate the ability of the LF to detect small changes in ω_n, as highlighted in Table 4, thus demonstrating the feasibility of the method for SHM. In addition, Figure 6 shows the effect of the three different damage scenarios, which, for conciseness' sake, includes only the modal parameters of the first three modes. Since ζ_n is left unchanged, Figures 6(a) and 6(b), respectively, portray the Δ changes (calculated according to equation (29)) between ω_{1-3} and plot ϕ_{1-3} between the estimated undamaged and damaged noiseless case. As shown, there is a clear relationship between the increase in damage and ω_{1-3}'s Δ and in ϕ_{1-3} trajectories. The

Table 4: 9 DoF system: natural frequencies, in Hz, of the numerical undamaged and damaged (5, 10, and 30%) cases.

	Natural frequency (Hz)			
Mode	Undamaged	5%	10%	30%
#1	1.859	1.855	1.851	1.827
#2	5.525	5.500	5.472	5.327
#3	9.041	9.040	9.039	9.030
#4	12.311	12.243	12.170	11.796
#5	15.244	15.235	15.226	15.176
#6	17.762	17.693	17.617	17.239
#7	19.795	19.737	19.677	19.433
#8	21.288	21.261	21.231	21.095
#9	22.201	22.098	22.010	21.784

difference between the baseline and damaged ω_{1-3} increases and the ϕ_{1-3} trajectory deviation gets more pronounced as the damage increases, as expected. This allows damage severity assessment in addition to damage detection. Moreover, the most significant deviation in the ϕ_n trajectories happens within the fifth node, thus allowing for the use of LF for damage localisation as well.

To summarise this set of results, the performance of the LF has been numerically evaluated for the detection of changes in ω_n and ϕ_n induced by progressive stiffness reductions. As preliminarily shown for the baseline scenario, the identification of the damaged scenarios is coherent with the expected values for low levels of noise. This translates to the possibility of using the extracted modal parameters for damage detection and localisation. As expected, the SI approach is able to track the decrease of ω_n caused by the stiffness reduction; the identified modal coordinates reflect ϕ_n's deviated trajectories, according to the severity and location of the damage. This proves that the LF is precise and robust enough to be used for damage detection in mechanical systems.

In the following section, the LF is again compared to N4SID, in the time domain, and to LSCE, in the frequency domain, to evaluate its SI and SHM capabilities on a benchmark experimental case study.

2.7. Experimental Case Study. Since the results presented for the numerical case demonstrate that the LF can be a feasible alternative for the SI and SHM of mechanical systems, this study is to test the reliability of the method against real data. The experimental case study selected to extensively test the LF's capabilities to detect and track changes in the mechanical properties of the system (both mass and stiffness), even under noisy conditions and with nonlinearities added to the system, is the well-known [45–48] three-storey frame structure benchmark experiment performed at the EI at the LANL [49, 50].

The three-storey structure, as shown in Figure 7, is made of four plates ($30.5 \times 30.5 \times 2.5$ cm) linked to columns ($17.7 \times 2.5 \times 0.6$ cm) by bolted joints. A small protrusion ($15.0 \times 2.5 \times 2.5$ cm) is suspended from the top floor part of a bumper-column system. This is intended to simulate nonlinear effects, mimicking a breathing crack mechanism [51], with its interaction with a bumper placed on the second floor (see the zoomed-in part in Figure 7). The base plate is constrained on rails that allow movement in the transverse direction only, which is also the direction of the input force acting on the base plate. The structure can be regarded as a 4 DoF system, with each DoF corresponding to a floor. For civil engineering purposes, this is a classic simplified model of shear-type multi-storey building. The frame structure and the shaker are mounted on the same baseplate ($76.2 \times 30.5 \times 2.5$ cm). The input force from the shaker to the structure is measured via a load cell with a nominal sensitivity of 2.2 $\mathrm{mVN^{-1}}$. Four accelerometers with nominal sensitivities of 1,000 $\mathrm{mVg^{-1}}$ are attached at the centerline of each floor. Data are collected and processed by the means of a Dactron Spectrabook and the shaker is driven by a Techron 5530 Power Supply Amplifier. The structure is excited with a band-limited random excitation in the range of 20–150 Hz. The lower limit is selected to avoid the rigid-body mode of the structure. A 2.6 V RMS in the Dactron system, approximately 20 N RMS measured at the input, is set as the excitation level.

Table 5 lists the 17 tested scenarios. The first is the baseline configuration, #2-#3 represent changes in environmental conditions by the means of adding mass, #4 to #9 represent stiffness reductions by changing column thickness, and #10 to #17 are nonlinear cases. The nonlinearity, as previously mentioned, is introduced with the extra columns and bumper, and it is regulated by the distance between the two. This causes a pointwise source of bilinear stiffness at the top floor, which is free to vibrate when moving in the positive x direction and constrained when moving in the opposite (negative) x direction. Notably, cases #10–14 are nonlinear-only configurations, while #15–17 are nonlinear and environmentally conditioned configurations. It is worth noting that LF is a *linear* SI method; hence, nonlinearity, for the scope of this work, is considered as a noise-like disturbance and not as a per se phenomenon. Hence, the identified parameters for this case refer to the underlying linear system and not to the bilinear stiffness induced by the bumper-stopper interaction. A total of 850 realisations, 50 for each case, exist, and this allowed for an exhaustive statistical comparison of the identification methods' results.

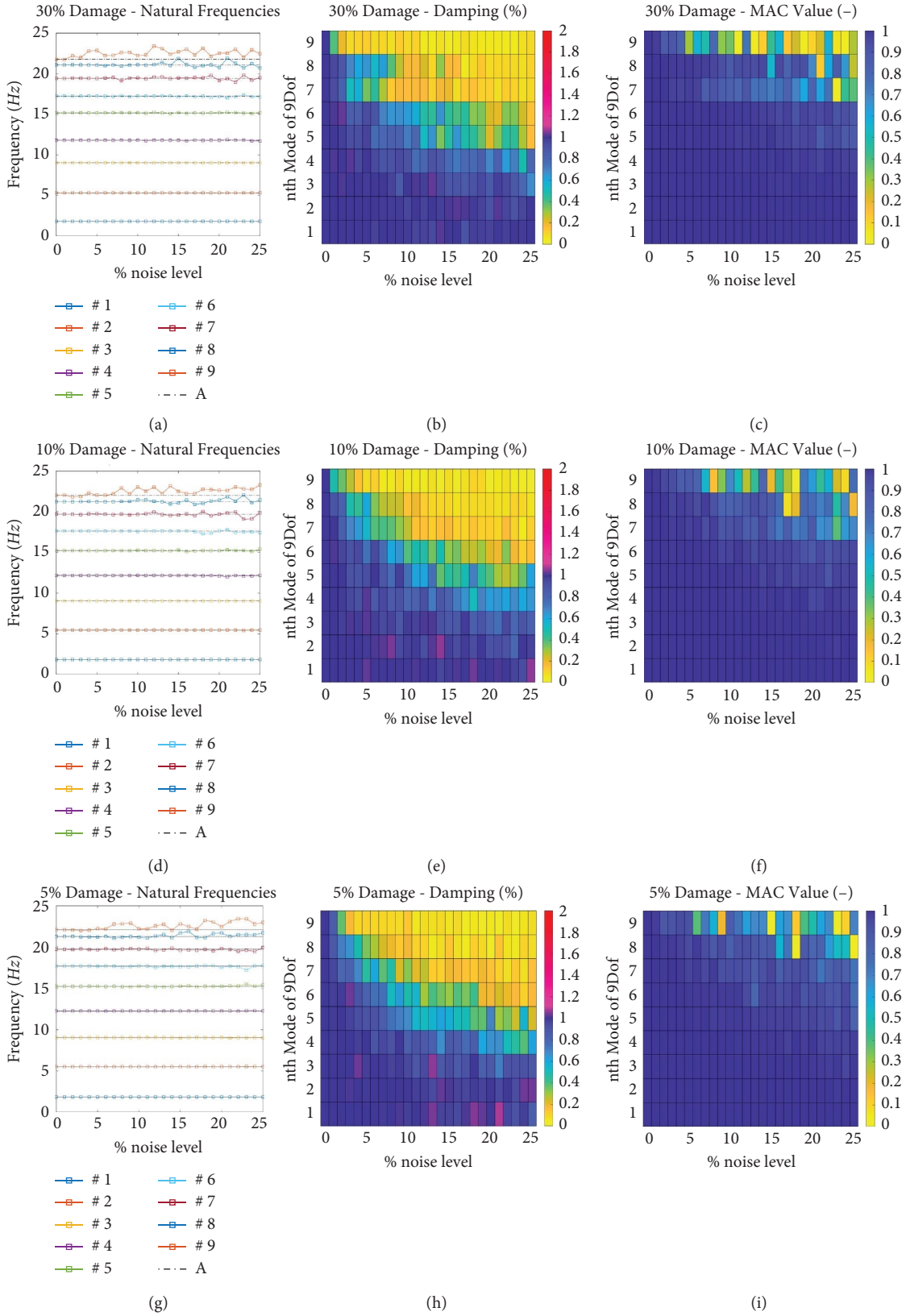

FIGURE 5: 9 DoF system: 30% damage (top), 10% damage (middle), and 5% damage (bottom) at position 6. Results of the numerical study on the numerical case affected by input-output noise. (a, d, g) Effects on ω_n identification. (b, e, h) Effects on ζ_n. (c, f, i) Effects on ϕ_n. In the legend, "A" indicates the numerical results and "#n" stands for mode #n.

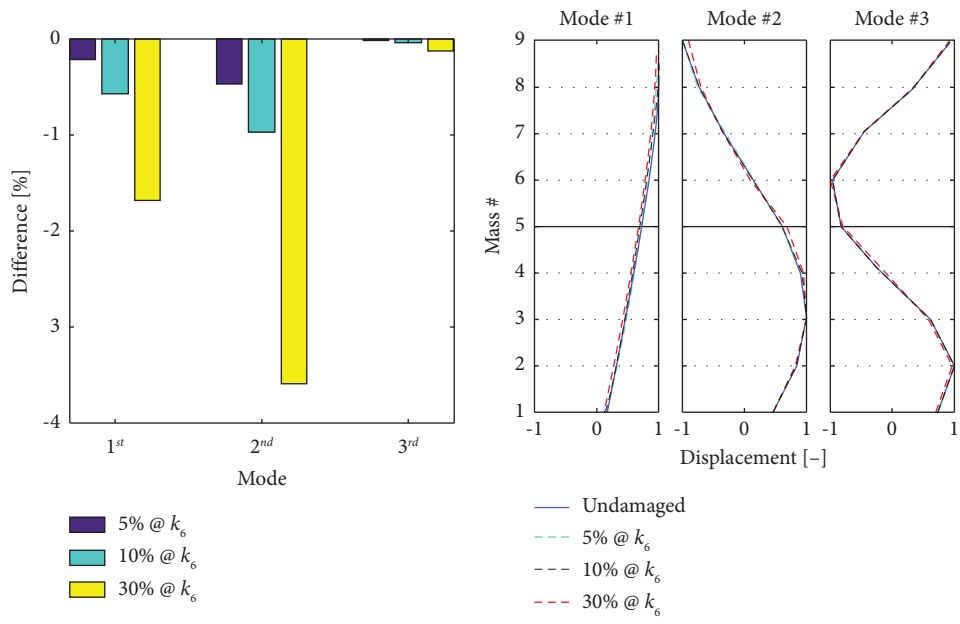

FIGURE 6: 9 DoF system: relative difference, in percentage, between baseline and damaged cases in ω_n for the first three modes (a) and the first three ϕ_n for the numerical baseline and damaged cases (b). The data refer to the noiseless case identified by LF, and the thicker grid line marks the damage location.

Each instance comes with a recorded input (in terms of force, N, time histories (THs)) and the four respective outputs (as acceleration THs, in g); consequently, 50 SIMO accelerance FRFs (considering all the available output channels) are at disposal for any of the 17 cases. For adherence with the *Système international* of units, the output's THs in g are converted to ms^{-2}.

For the scope of this work, the first peak in the frequency-domain response of the three-storey structure is not considered because (as reported in the literature [49, 50]) it is not a vibration mode but actually a rigid-body motion, for which there is no interest for the proposed applications of the LF.

3. Results

In Figure 8, the Loewner realisation corresponding to the lowest order, $k = 6$, is compared with the accelerance FRF of selected cases, in this instance, scenarios #1, #4, and #14—hence, taking under consideration the baseline scenario, a damaged linear scenario, and a nonlinear scenario. This comparison features a single instance of a given scenario for conciseness. Table 6 presents the mean, μ, values of the identified ω_n and ζ_n for the three cases of interest in Figure 8, alongside benchmark [50] and literature [6] values, identified via FRVF. Table 6 and Figure 9 present the modal parameters identified by the LF, LSCE, and N4SID for the selected cases. The identified ω_n and ζ_n are statistically analysed in the boxplots of Figure 10, where LF results are also measured against the value obtained by N4SID. Lastly, Figure 11 compares Δ, as per equation (29), between the identified ω_n and ζ_n values of three damaged cases, #4, #5, and #9, and the baseline scenario, case #1, and Figure 12 plots ϕ_n of the cases just mentioned.

Figure 8 presents the results of the LF fitting over the accelerance FRFs of a single instance of cases #1 (Figure 8(a)), 4 (Figure 8(b)), and 14 (Figure 8(c)). For all cases shown, the maximum deviation (green line) is, by an order of magnitude, less than unity for the gain amplitude. The red dashed line represents the Loewner realisation, and the blue line represents the accelerance FRFs. Both amplitude and phase seem to be correctly modelled by the LF; nevertheless, case #14 shows that the noising effect of nonlinearity has a tangible effect on LF, particularly on phase modelling.

As can be seen in Table 6, ω_n values are very close for the three methods; nevertheless, ζ_n identification is not consistent for the last case for the LF. In fact, case #14's ζ_n is underestimated by the LF if compared with N4SID and LSCE. As it will be discussed in depth later, this is also the case with the other nonlinear scenarios. It should be noted that for the three cases under scrutiny, LSCE overestimates ζ_{1-2}, compared to N4SID. A good agreement is detected between the modal parameters identified via LF within this paper and the benchmark and literature results.

Nevertheless, the LF is able to correctly identify the three ϕ_n of the nonrigid-body modes of the three-storey structure,

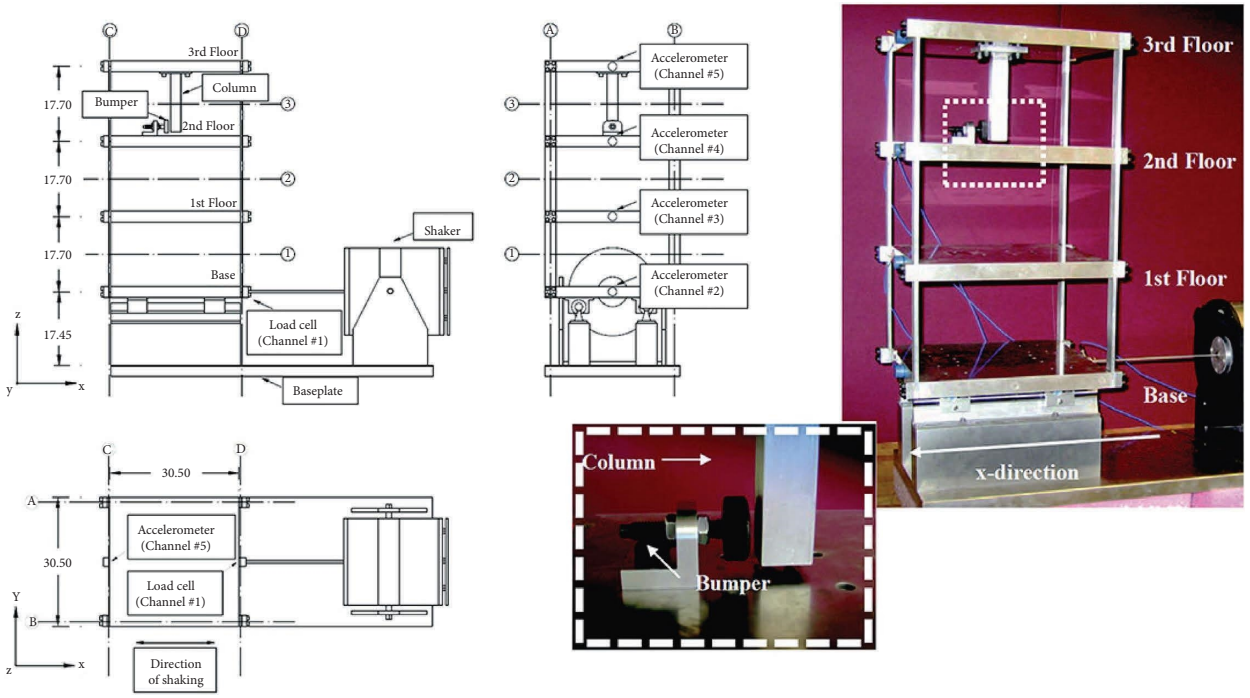

FIGURE 7: Three-storey frame structure: experimental test setup and schematic diagrams of the three-storey frame structure (adapted from [6, 49]).

TABLE 5: Three-storey frame structure: damage scenarios.

Case	Description
#1	Linear baseline
#2	Linear, added mass of 1.2 kg at the base
#3	Linear, added mass of 1.2 kg at the first floor
#4	Linear, 87.5% stiffness reduction in one column of the first interstorey
#5	Linear, 87.5% stiffness reduction in two columns of the first interstorey
#6	Linear, 87.5% stiffness reduction in one column of the second interstorey
#7	Linear, 87.5% stiffness reduction in two columns of the second interstorey
#8	Linear, 87.5% stiffness reduction in one column of the third interstorey
#9	Linear, 87.5% stiffness reduction in two columns of the third interstorey
#10	Nonlinear, distance between bumper and column tip: 0.20 mm
#11	Nonlinear, distance between bumper and column tip: 0.15 mm
#12	Nonlinear, distance between bumper and column tip: 0.13 mm
#13	Nonlinear, distance between bumper and column tip: 0.1 mm
#14	Nonlinear, distance between bumper and column tip: 0.05 mm
#15	Nonlinear, bumper 0.20 mm from column tip, 1.2 kg added at the base
#16	Nonlinear, bumper 0.20 mm from column tip, 1.2 kg added on the first floor
#17	Nonlinear, bumper 0.1 mm from column tip, 1.2 kg added on the first floor

as shown in Figure 9. The values plotted are the μ values of the identified modal displacements for each method. The blue solid line represents the N4SID identification, the red dashed line represents LF, and the black dashed-dotted line represents LSCE. The coherence within the ϕ_n is confirmed by the MAC matrix diagonal values between the identified ϕ_n (N4SID vs. LSCE, N4SID vs. LF, and LSCE vs. LD) being very close to unity, thus showing an almost perfect correlation.

Lastly, the results of the LF identification of the 850 instances are compared to the μ values of the corresponding N4SID identification in Figure 10. In Figures 10(a) and 10(b), the median value is represented by the central red line. The bottom and top blue edges of the box plots represent the 25th and 75th percentiles, while the whiskers are the largest and smallest data points not considered as outliers, and the red Greek cross indicates the outlier values. These metrics give statistical significance to the parameters identified via the LF. The identified ω_n values match their N4SID-identified counterparts, while for ζ_n, the LF match with N4SID results is less ideal. Generally, the LF underestimates in all scenarios of ζ_n, when compared to N4SID; nevertheless, the difference is small, except for cases #5, #13, and #14. Cases #13 and #14 also show the biggest difference between their 25th

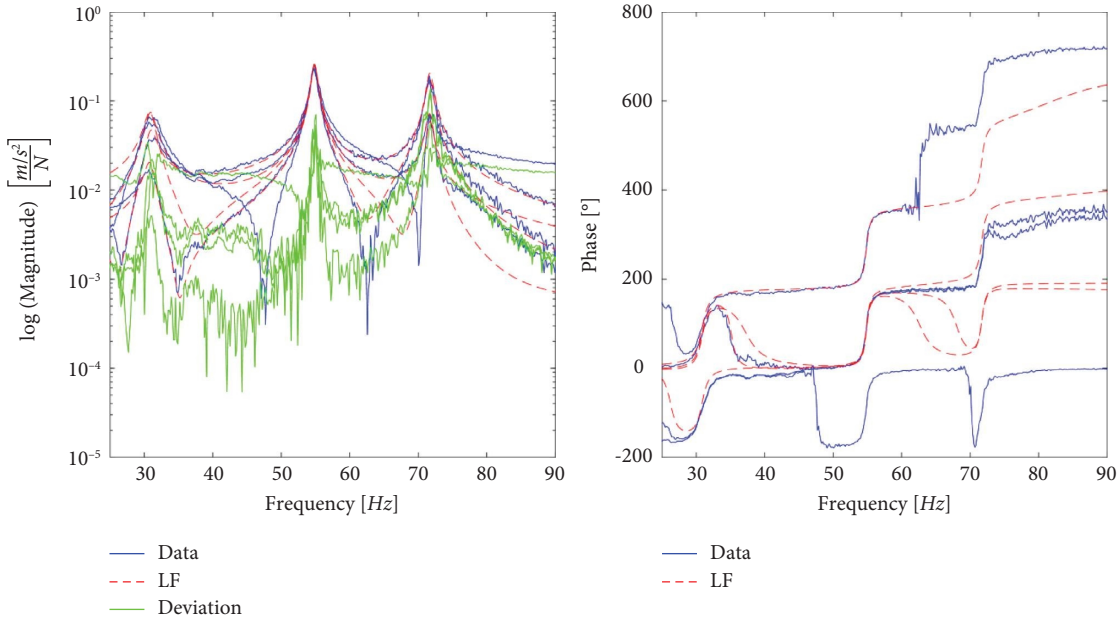

(a)

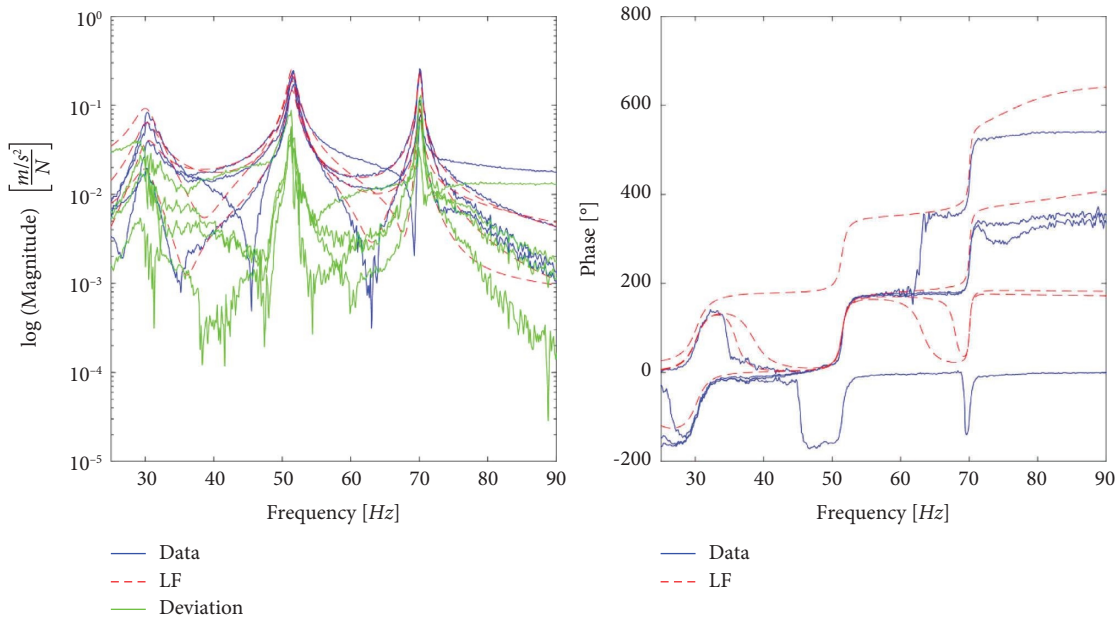

(b)

Figure 8: Continued.

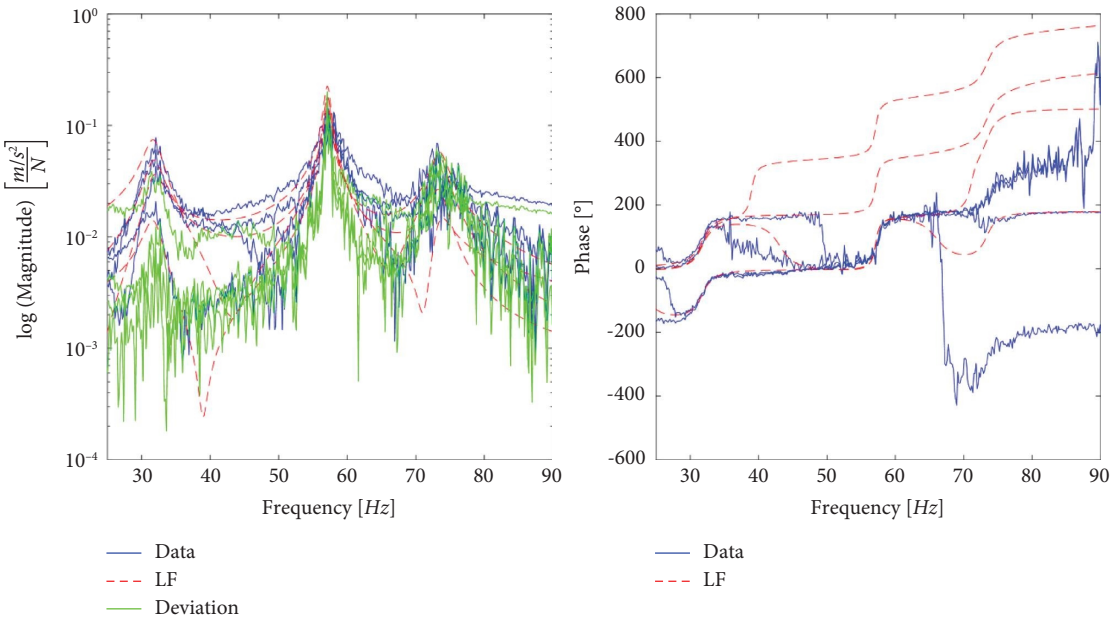

(c)

FIGURE 8: Three-storey structure: the FRF computed from the test data is compared with the LF's transfer function, for a single instance of cases #1 (a), 4 (b), and 14 (c). The absolute gain (left) and the phase angle (left) are presented with all 4 channels superimposed for conciseness.

TABLE 6: Three-storey structure: identified ω_n, in Hz, and ζ_n of scenarios #1, 4, and 14 from benchmark [49], literature (FRVF [6]), N4SID, LSCE, and LF.

Scenario	Mode#	2	3	4	Scenario	Mode#	2	3	4
	Benchmark	30.700	54.200	70.100		Benchmark	0.063	0.020	0.010
	FRVF	30.890	54.740	71.610		FRVF	0.034	0.008	0.007
#1	N4SID	30.980	54.731	71.542	#1	N4SID	0.033	0.008	0.006
	LSCE	30.992	54.594	71.432		LSCE	0.038	0.014	0.007
	LF	30.986	54.751	71.574		LF	0.029	0.007	0.006
	Benchmark	30.900	51.200	69.200		Benchmark	0.071	0.022	0.006
	FRVF	30.650	51.540	70.050		FRVF	0.036	0.009	0.004
#4	N4SID	30.742	50.919	70.026	#4	N4SID	0.033	0.011	0.003
	LSCE	30.735	51.103	70.041		LSCE	0.038	0.015	0.003
	LF	30.700	51.532	70.013		LF	0.028	0.009	0.003
	Benchmark	33.500	57.600	74.200		Benchmark	0.071	0.022	0.010
	FRVF	31.730	56.980	73.710		FRVF	0.530	0.055	0.030
#14	N4SID	31.520	57.532	72.872	#14	N4SID	0.035	0.018	0.017
	LSCE	32.093	57.886	73.886		LSCE	0.035	0.019	0.009
	LF	31.667	57.577	73.110		LF	0.016	0.005	0.001

and 75th percentiles for ω_n. The cause of this issue can be traced back to the high nonlinearity of these two cases, which is perceived as noise by the LF, which is sensitive to high noise levels. In general, identified ω_n are quite stable, except for the mentioned cases. This stability is less pronounced for ζ_n, particularly for the first nonrigid-body mode.

Figure 11 shows Δ between cases #4, #5, and #9 and the baseline case, #1. Cases #4 and #5 are two similar damaged cases. The former has a stiffness reduction in one column of the first interstorey, and the latter has a stiffness reduction in two columns of the same interstorey. Hence, their damage differs only in severity rather than localisation, which is the case for case #9: featuring a stiffness reduction in two columns of the third interstorey. These facts are well represented in Figure 11(a), as Δ of the identified ω_n increase between cases #4 and #5 and case #9 experiences a negative Δ, as expected in a damaged scenario. Figure 11(b) reports on Δ between identified ζ_n in the damaged cases and the baseline cases. However, it is well known that changes in modal damping generally provide little useful information for damage detection. In fact, no strong correlation between $\Delta\zeta_n$ and increasing damage is visible, independently of the considered system identification algorithm.

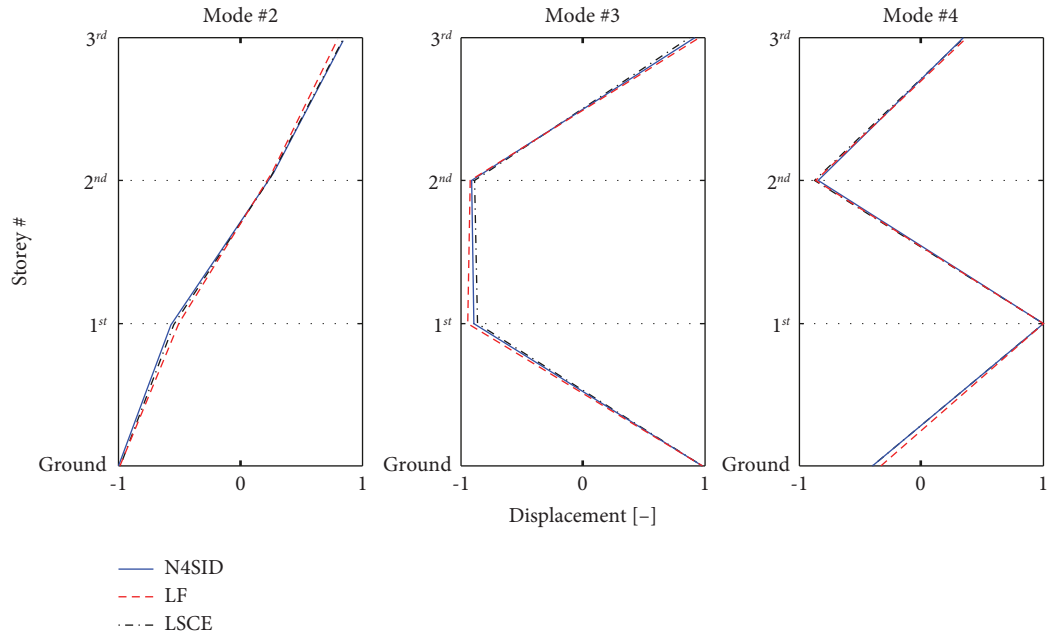

FIGURE 9: Three-storey structure: mode shapes of nonrigid-body motion modes identified via N4SID, LSCE, and LF.

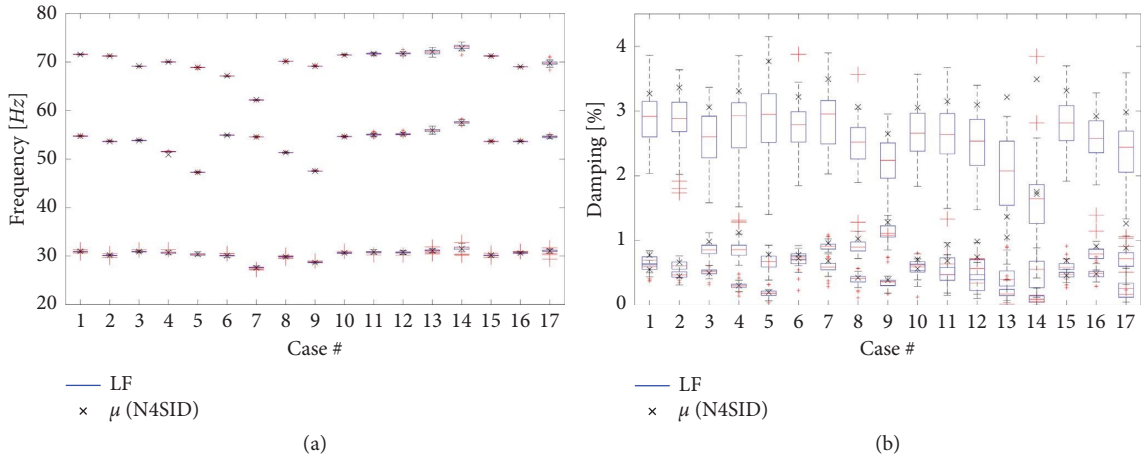

FIGURE 10: Three-storey structure: box plot of ω_n (a) and ζ_n (b) for each case (over 50 instances). The median value is represented by the central red line, the bottom and top blue edges of the box indicate the 25th and 75th percentiles, and the whiskers are the largest and smallest data points not considered as outliers. The red plus symbol indicates the outlier values. The black saltire represents the values identified via N4SID.

Finally, Figure 12 plots the identified ϕ_n of the baseline and the damaged cases #4, #5, and #9. The difference in values between the data from cases #4 and #5 increases with damage, but the mode shape still retains the same trajectory, as expected for a decrease of stiffness, while for case #9, the variation is more consistent, as a pointwise source of nonlinearity is added at the top floor.

To summarise the experimental validation, the extensive benchmark dataset of the three-storey frame structure allowed for a thorough validation of the SI procedure for the precise extraction of modal parameters with different levels of increasing damage. The modal parameters extracted via LF are generally coherent to those extracted by N4SID, LSCE, and FRVF, as well as to the benchmark results reported in the scientific literature. This is particularly valid for all the ω_n and ϕ_n values. In sparse occasions, the benchmark ζ_n results are not fully coherent with the LF-identified parameters; however, this is also true for N4SID, LSCE, and FRVF results.

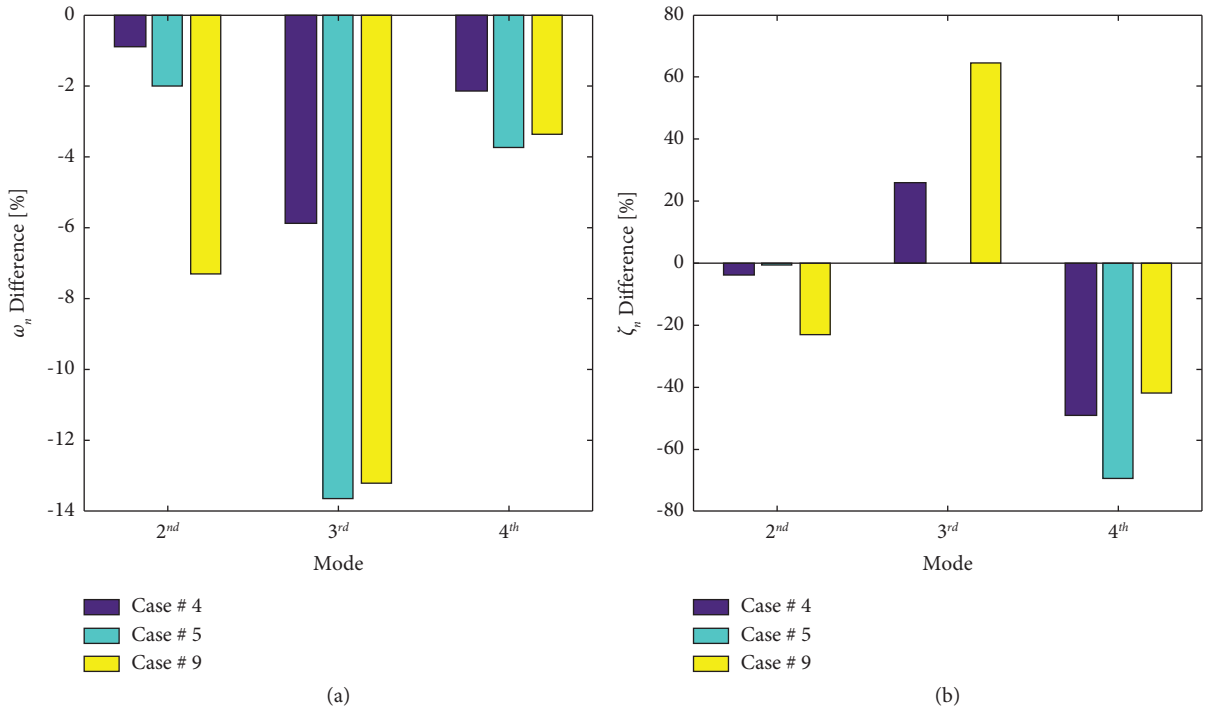

FIGURE 11: Three-storey structure: ω_n (a) and ζ_n (b) of the undamaged and damaged settings. The y-axis indicates the relative change (Δ) in percentage.

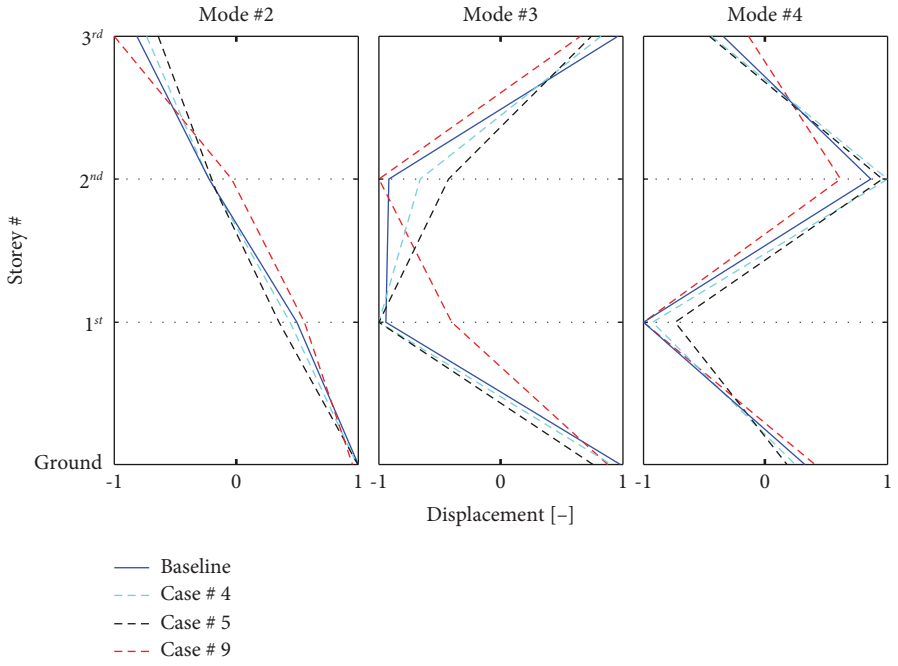

FIGURE 12: Three-storey structure: ϕ_n of the undamaged and damaged (cases #4, 5, and 9) settings.

Hence, the precision of the LF-identified modal parameters allows for damage severity assessment and localisation, at least to the same extent as the other three techniques.

4. Conclusions

In this work, the suitability of the LF as an input-output SI method for the extraction of modal parameters has been numerically and experimentally verified. Furthermore, the viability of such precise estimates for damage detection has been investigated as well, applying them to classic SHM procedures. To the authors' best knowledge, this work is the first attempt at extracting modal parameters (ω_n, ζ_n, and ϕ_n) via LF and also the first application of LF for SHM purposes.

First, the LF has been validated with a numerical model of a 9 DoF system against the same parameters as identified via N4SID and LSCE. This displayed the limitations of LSCE for closely spaced modes, while instead proving the accuracy and precision of the LF. Furthermore, an investigation of the effects of measurement noise has been carried out on the same numerical case study, also considering the case of developing damage. The signals have been corrupted with AWGN. For damage detection purposes, three damaged scenarios (5%, 10%, and 30% stiffness reduction on the fifth element) have been generated. The LF correctly identified the modal parameters and found the differences between different damage states.

Lastly, the LF has been compared to N4SID and LSCE on an experimental three-storey frame structure dataset from LANL, which features 17 different structural scenarios. Once again, the LF reliably returned the modal parameters of the structure under investigation, even with noisy measurement and/or in presence of damage-induced nonlinearities, such as for cases #14–17. These identifications were found to be accurate enough to allow for damage detection, localisation, and severity assessment and thus for a full damage diagnosis and assessment procedure.

To summarise the main findings, the main advantage of the LF over the existing methods, in particular over LSCE, is a more consistent ζ_n estimation. It must be said that, as it happens for similar techniques, ζ_n remains the most difficult modal parameter to estimate accurately. The results for the three-storey structure show great agreement with the benchmark values and those available in the scientific literature.

Another point to consider is that the identification is more influenced by output noise rather than input noise; therefore, accurate sensing devices should be used, as usual for any experimental setup. Given the requirement for precise and accurate modal parameters for SHM and considering the aforementioned results and discussion, the LF is clearly validated for SI and SHM applications to mechanical systems. The only real practical limitation for LF lies in being an input-output method, which is generally less practical than output-only approaches for the OMA of large structures. This aspect will be addressed in future works.

Data Availability

The experimental data used to support the findings of this study are available in the Engineering Institute at Los Alamos National Laboratory website at https://www.lanl.gov/projects/national-security-education-center/engineering/ei-software-download/index.php (data file 1), and more data that support this study (data file 2) can be accessed through the Cranfield University repository (CORD) at https://doi.org/10.17862/cranfield.rd.16636279. This project contains the following underlying data: data file 1—the three-storey structure dataset from the Engineering Institute at Los Alamos National Laboratory; data file 2—a tutorial on the Loewner framework for mechanical systems. Data file 2 is available under the terms of the Creative Commons Attribution 4.0 International (CC BY 4.0).

Conflicts of Interest

The authors declare that there are no conflicts of interest regarding the publication of this paper.

Acknowledgments

The authors would like to thank LANL for providing the experimental data used in this article as well as Prof. Stefano Grivet-Talocia of the Department of Electronics and Telecommunications of the Politecnico di Torino and Dr. Alessandro Pontillo of the Department of Aerospace Engineering of the University of Bristol for their valued advice. The authors from Cranfield University disclosed receipt of the following financial support for the research, authorship, and/or publication of this article: this study was supported by the Engineering and Physical Sciences Research Council (EPSRC) (grant no. 2277626).

References

[1] C. R. Farrar, S. W. Doebling, and D. A. Nix, "Vibration–based structural damage identification," *Philosophical Transactions of the Royal Society of London,Series A: Mathematical, Physical and Engineering Sciences*, vol. 359, no. 1778, pp. 131–149, 2001.

[2] A. Rytter, "Vibrational Based Inspection of Civil Engineering Structures," PhD Thesis, Aalborg University, Aalborg Øst, Denmark, 1993.

[3] G. Dessena, D. I. Ignatyev, J. F. Whidborne, A. Pontillo, and L. Zanotti Fragonara, "Ground vibration testing of a flexible wing: a benchmark and case study," *Aerospace*, vol. 9, no. 8, p. 438, 2022.

[4] M. Civera, V. Mugnaini, and L. Zanotti Fragonara, "Machine Learning-based Automatic Operational Modal Analysis: A Structural Health Monitoring Application to Masonry Arch Bridges," *A Structural Health Monitoring*, vol. 29, pp. 1–23, 2022.

[5] M. Richardson and B. Schwarz, "Modal Parameter Estimation from Operating Data," *Sound and Vibration Magazine*, 2003.

[6] M. Civera, G. Calamai, and L. Zanotti Fragonara, "Experimental modal analysis of structural systems by using the fast

relaxed vector fitting method," *Structural Control and Health Monitoring*, vol. 28, no. 4, pp. 1–23, Apr. 2021.

[7] M. Civera, G. Calamai, and L. Zanotti Fragonara, "System identification via fast relaxed vector fitting for the structural health monitoring of masonry bridges," *Structures*, vol. 30, pp. 277–293, Apr. 2021.

[8] M. T. A. Chaudhary and Y. Fujino, "System identification of bridges using recorded seismic data and its application in structural health monitoring," *Structural Control and Health Monitoring*, vol. 15, no. 7, pp. 1021–1035, 2008.

[9] X. Zhi-Qian, P. Jian-Wen, W. Jin-Ting, and C. Fu-Dong, "Improved approach for vibration-based structural health monitoring of arch dams during seismic events and normal operation," *Structural Control and Health Monitoring*, vol. 29, no. 7, Article ID e2955.

[10] S. Lefteriu and A. C. Antoulas, "Modeling multi-port systems from frequency response data via tangential interpolation," in *Proceedings of the 2009 IEEE Workshop on Signal Propagation on Interconnects*, pp. 1–4, Naples, Italy, May 2009.

[11] S. Lefteriu and A. C. Antoulas, "A new approach to modeling multiport systems from frequency-fomain data," *IEEE Transactions on Computer-Aided Design of Integrated Circuits and Systems*, vol. 29, no. 1, pp. 14–27, Jan. 2010.

[12] A. C. Ionita, "System identification," 2013, http://aci.rice.edu/system-identification/.

[13] D. L. Brown, R. J. Allemang, R. Zimmerman, and M. Mergeay, "Parameter estimation techniques for modal analysis," *Automotive Engineering Congress and Exposition*, vol. 19, Article ID 790221, 1979.

[14] L. Zadeh, "On the identification problem," *IEEE Transactions on Circuit Theory*, vol. 3, no. 4, pp. 277–281, 1956.

[15] P. van Overschee and B. de Moor, "N4SID: subspace algorithms for the identification of combined deterministic-stochastic systems," *Automatica*, vol. 30, no. 1, pp. 75–93, 1994.

[16] F. Dezi, F. Gara, and D. Roia, "Dynamic characterization of open-ended pipe piles in marine environment," in *Applied Studies of Coastal and Marine Environments*InTech, London, UK, 2016.

[17] F. R. Spitznogle and A. H. Quazi, "Representation and analysis of time-limited signals using a Complex Exponential algorithm," *Journal of the Acoustical Society of America*, vol. 47, no. 5, pp. 1150–1155, 1970.

[18] F. R. Spitznogle, J. M. Barrett, C. I. Black, T. W. Ellis, and W. L. LaFuze, "Representation and analysis of sonar signals," *Improvements in the Complex Exponential signal analysis computational algorithm*, 1971.

[19] N. M. M. Maia, "Extraction of Valid Modal Properties from Measured Data in Structural Vibrations," PhD Thesis, Imperial College London, London, UK, 1988.

[20] L. Gelman, I. Petrunin, C. Parrish, and M. Walters, "Novel health monitoring technology for in-service diagnostics of intake separation in aircraft engines," *Structural Control and Health Monitoring*, vol. 27, no. 5, pp. 1–14, 2020.

[21] P. Rizzo and A. Enshaeian, "Challenges in bridge health monitoring: a review," *Sensors*, vol. 21, no. 13, p. 4336, 2021.

[22] F. M. Hemez and S. W. Doebling, "Review and assessment of model updating for non-linear, transient dynamics," *Mechanical Systems and Signal Processing*, vol. 15, no. 1, pp. 45–74, Jan. 2001.

[23] N. F. Alkayem, M. Cao, Y. Zhang, M. Bayat, and Z. Su, "Structural damage detection using finite element model updating with evolutionary algorithms: a survey," *Neural Computing & Applications*, vol. 30, no. 2, pp. 389–411, 2018.

[24] G. Dessena, D. I. Ignatyev, J. F. Whidborne, and L. Zanotti Fragonara, "A kriging approach to model updating for damage detection," in *EWSHM 2022, LNCE 254*, P. Rizzo and A. Milazzo, Eds., Springer, Singapore, pp. 245–255, 2023.

[25] A. Cancelli, S. Laflamme, A. Alipour, S. Sritharan, and F. Ubertini, "Vibration-based damage localization and quantification in a pretensioned concrete girder using stochastic subspace identification and particle swarm model updating," *Structural Health Monitoring*, vol. 19, no. 2, pp. 587–605, Mar. 2020.

[26] W. Fan and P. Qiao, "Vibration-based damage identification methods: a Review and comparative study," *Structural Health Monitoring*, vol. 10, no. 1, pp. 83–111, Jan. 2011.

[27] E. Reynders, R. Pintelon, and G. de Roeck, "Uncertainty bounds on modal parameters obtained from stochastic subspace identification," *Mechanical Systems and Signal Processing*, vol. 22, no. 4, pp. 948–969, May 2008.

[28] D. Quero, P. Vuillemin, and C. Poussot-Vassal, "A generalized state-space aeroservoelastic model based on tangential interpolation," *Aerospace*, vol. 6, no. 1, p. 9, 2019.

[29] M. H. Richardson and D. L. Formenti, "Global curve fitting of frequency response measurements using the rational fraction polynomial method," *Proceedings of the International Modal Analysis Conference & Exhibit*, vol. 1, pp. 390–397, 1985.

[30] B. Gustavsen, "Relaxed vector fitting algorithm for rational approximation of frequency domain responses," *IEEE Workship on Signal Propagation on Interconnects*, vol. 1, pp. 97–100, 2006.

[31] B. Gustavsen and A. Semlyen, "Rational approximation of frequency domain responses by vector fitting," *IEEE Transactions on Power Delivery*, vol. 14, no. 3, pp. 1052–1061, 1999.

[32] A. C. Antoulas, S. Lefteriu, and A. C. Ionita, "Chapter 8: a tutorial introduction to the loewner framework for model reduction," in *Model Reduction and Approximation*Society for Industrial and Applied Mathematics, Philadelphia, PA, USA, 2011.

[33] D. S. Karachalios, I. V. Gosea, and A. C. Antoulas, "The Loewner framework for nonlinear identification and reduction of Hammerstein cascaded dynamical systems," *Proceedings in Applied Mathematics and Mechanics*, vol. 20, no. 1, pp. 2020–2022, 2021.

[34] K. Löwner, "Uber monotone matrixfunktionen," *Mathematische Zeitschrift*, vol. 38, no. 1, pp. 177–216, Dec. 1934.

[35] B. D. O. D. O. Anderson and A. C. C. Antoulas, "Rational interpolation and state-variable realizations," *Linear Algebra Appl*, vol. 137–138, pp. 479–509, 1990.

[36] A. C. Antoulas, "A tutorial introduction to the Loewner framework for model reduction," in *Proceedings of the 9th Elgersburg Workshop Mathematische Systemtheorie*, Stuttgart, Germany, October 2014.

[37] A. J. J. Mayo and A. C. C. Antoulas, "A framework for the solution of the generalized realization problem," *Linear Algebra Appl*, vol. 425, no. 2–3, pp. 634–662, Sep. 2007.

[38] J. Meinguet, *On the solubility of the Cauchy interpolation problem*, A. Talbot, Ed., Approximation Theory, Academic Press, New York, USA, 1969.

[39] C. Schneider and W. Werner, "Some new aspects of rational interpolation," *Mathematics of Computation*, vol. 47, no. 175, p. 285, 1986.

[40] B. Kramer and S. Gugercin, "Tangential interpolation-based eigensystem realization algorithm for MIMO systems," *Mathematical and Computer Modelling of Dynamical Systems*, vol. 22, no. 4, pp. 282–306, 2016.

[41] G. Dessena, *A Tutorial on the Loewner-Based System Identification and Structural Health Monitoring Approach for Mechanical Systems*, Cranfield University, Cranfield, UK, 2022.

[42] L. A. A. Bull, "Foundations of population-based SHM, Part I: homogeneous populations and forms," *Mechanical Systems and Signal Processing*, vol. 148, Article ID 107141, 2021.

[43] D. J. Ewins, *Modal Testing Theory, Practice and Application*, Research Studies Press, Baldock, UK, 2 edition, 2000.

[44] R. J. Allemang and D. L. Brown, "A correlation coefficient for modal vector analysis," in *Proceedings of the 1st International Modal Analysis Conference*, pp. 110–116, Orlando, Fl, USA, November 1982.

[45] M. Civera and C. Surace, "Instantaneous spectral entropy: an application for the online monitoring of multi-storey frame structures," *Buildings*, vol. 12, no. 3, p. 310, Mar. 2022.

[46] M. Civera and C. Surace, "A comparative analysis of signal decomposition techniques for structural health monitoring on an experimental benchmark," *Sensors*, vol. 21, no. 5, 2021.

[47] D. Martucci, M. Civera, and C. Surace, "The extreme function theory for damage detection: an application to civil and aerospace structures," *Applied Sciences*, vol. 11, no. 4, 2021.

[48] M. Civera, M. Ferraris, R. Ceravolo, C. Surace, and R. Betti, "The teager-kaiser energy cepstral coefficients as an effective structural health monitoring tool," *Applied Sciences*, vol. 9, no. 23, 2019.

[49] E. Figueiredo, G. Park, J. Figueiras, C. Farrar, and K. Worden, *Structural Health Monitoring Algorithm Comparisons Using Standard Data Sets*, Los Alamos, NM, USA, 2009.

[50] E. Figueiredo, G. Park, C. R. Farrar, K. Worden, and J. Figueiras, "Machine learning algorithms for damage detection under operational and environmental variability," *Structural Health Monitoring*, vol. 10, no. 6, pp. 559–572, 2011.

[51] A. Bovsunovsky and C. Surace, "Non-linearities in the vibrations of elastic structures with a closing crack: a state of the art review," *Mechanical Systems and Signal Processing*, vol. 62, no. 63, pp. 129–148, Oct. 2015.